A generalised plate with kinematically independent thickness for modelling shapes of corneas affected by keratoconus before and after penetrating keratoplasty

Francesco dell'Isola
Department of Civil, Construction-Architectural and Environmental Engineering, University of L'Aquila, L'Aquila, Italy; International Research Center for the Mathematics and Mechanics of Complex Systems, MeMoCS, University of L'Aquila, L'Aquila, Italy

Francesco D'Annibale
Department of Civil, Construction-Architectural and Environmental Engineering, University of L'Aquila, L'Aquila, Italy; International Research Center for the Mathematics and Mechanics of Complex Systems, MeMoCS, University of L'Aquila, L'Aquila, Italy

Raimondo Luciano
Department of Engineering, Parthenope University of Naples, Napoli, Italy

Thomas Henze
Auge und Sehen Henze UG (haftungsbeschränkt), Nürnberg, Germany

Ivan Giorgio
Department of Civil, Construction-Architectural and Environmental Engineering, University of L'Aquila, L'Aquila, Italy; International Research Center for the Mathematics and Mechanics of Complex Systems, MeMoCS, University of L'Aquila, L'Aquila, Italy

Abstract
A two-dimensional (2D) reduced-order generalised continuum model within the framework of the three-dimensional (3D) deformations is deduced from a 3D Cauchy continuum model by imposing a micro-macro kinematical map, which is linear in the direction normal to the corneal surface. This kinematical assumption is plausible as the cornea thickness

is much smaller than its diameter. We use the obtained 2D generalised continuum that incorporates a kinematically independent thickness to model the changes of shape induced in corneas: (1) by the changes of cornea mechanical properties whose aetiology can be found in the complex (and not completely understood yet) pathogenic process causing keratoconus, (2) by penetrating keratoplasty, and (3) degeneration of both patient residual corneal tissue and transplanted corneal tissue after transplant. We postulate that growth and regeneration phenomena occurring in the cornea shape it following the "elastic" solutions, which we have calculated. The preliminary obtained predictions seem to promise significant applicative developments and are in good qualitative agreement with experimental results: future investigations will need to improve the presented model by considering explicitly the remodelling phenomena and a more detailed analysis of the evolution of metabolically driven mechanical damage of corneal tissue and its visco-plasticity.

Keywords
Generalized continua, 2D reduced models, cornea pathologies, penetrating keratoplasty, biomechanics

1. Introduction

The structure of the cornea has been extensively investigated in the literature for a long time (see, e.g., the fundamental work [1] focusing on keratoconus). Here, we give a short description of some of the works on the subject that are available in the literature and relevant to the present modelling effort. Very appropriate for the modelling of corneal mechanical properties, needed here, are the papers [2–4], which formulate, in a mechanically precise language, the available knowledge about the physiology of human corneas. Some preliminary results relating to those contained in this paper were presented in the work by dell'Isola et al. [5]: the very interesting and fruitful discussions with the co-authors of that presentation are explicitly acknowledged here.

1.1. A short description of corneal structure

The corneal tissue has a complex microstructure. Here, we quote the fundamental anatomical facts on which we base our modelling assumptions.

In Figure 1, we show schematically the anatomy of the anterior part of the human eye: the orange part is the vitreous body, which allows the light rays to react with the posterior part of the eye, where the retina is located.

Zooming in for a close-up of the layer, which is called the cornea, we can distinguish several different layers, all of which play a role in the onset and development of keratoconus. In this preliminary modelling analysis, we assume, for these layers, a unique three-dimensional (3D) continuous model, and we account for its microstructure by means of suitable inhomogeneities of the constitutive equations for the fourth-order linear elasticity tensor (see the following sections for more details), used in 3D Cauchy elastic continua.

In Figure 1, we show a schematic picture of the different corneal layers, which, all together, constitute the corneal tissue. Once initiated, the keratoconus development is related to the progressive dissolution of Bowman's layer (located, see Figure 1 again, between the corneal epithelium and the stroma): for more details about this point, the reader can consult the work by [6].

In the degenerative process leading to keratoconus, another important mechanical and geometrical property of the cornea plays a relevant role: the cornea thickness.

In Figure 2, we show two contour plots for the same cornea affected by keratoconus. It has to be remarked that while the curvature of the outer corneal surface is concentrated around a point displaced below (in the direction of the weight), the thickness is rather symmetrical around the central point of the cornea. As the degeneration (decrease) of corneal elastic moduli is most likely correlated to the reduction in corneal thickness, we conjecture that the externally applied loads (such as the interaction with eyelids and the weight of both the cornea and the aqueous humour in contact with it) play a role in the observed shape of corneas affected by keratoconus due to the resultant shear stress on the cornea. This statement will be proved by means of numerical simulations in the following sections.

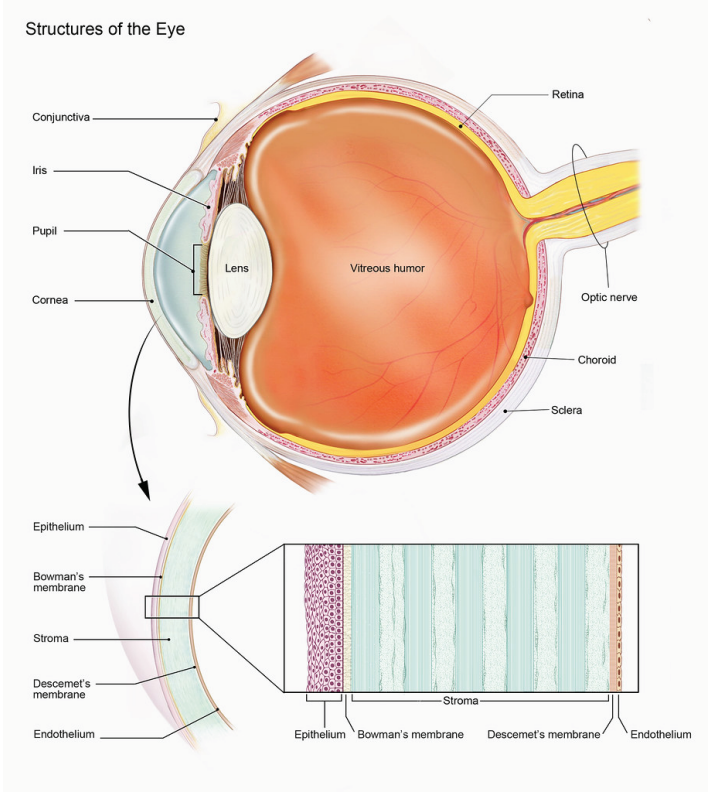

Figure 1. A schematic representation of the anatomy of the human eye with a magnified view of the corneal layers. Photo by National Institutes of Health (NIH), licensed under CC BY-NC 2.0.

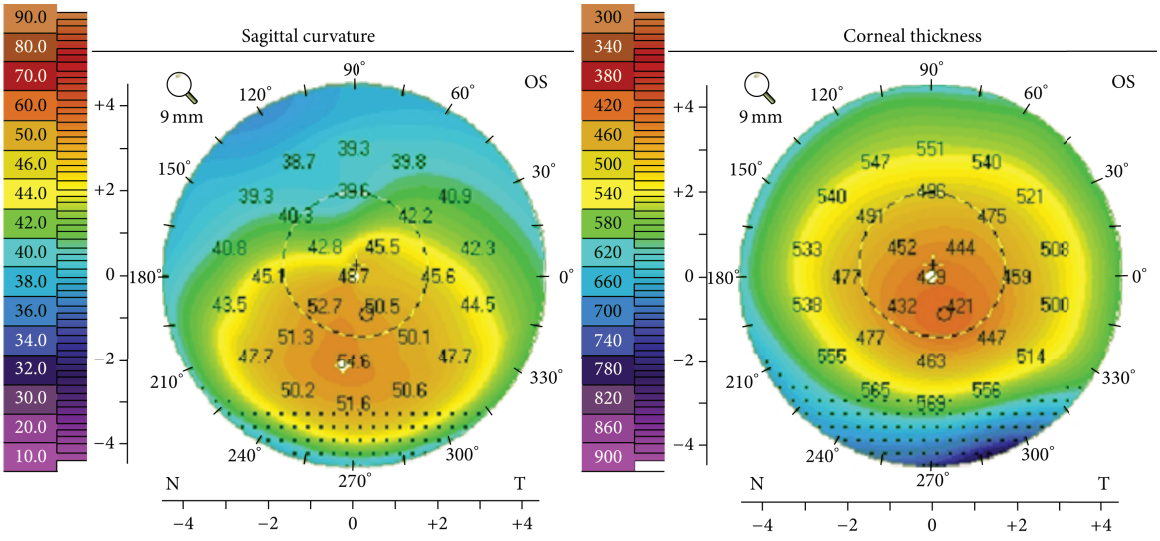

Figure 2. Typical corneal curvature and thickness in a keratoconus case.

1.2. Etiology and shape deformations induced by keratoconus

We have found it very useful to consult the fundamental paper [7]: when no explicit reference is given, we mean that we obtained from it the information reported below.

The influence of, at least, six genes has been found, up to now, to be associated with the onset of keratoconus: these genes include BANP-ZNF469, COL4A4, FOXO1, FNDC3B, IMMP2L, and RXRA-COL5A1,

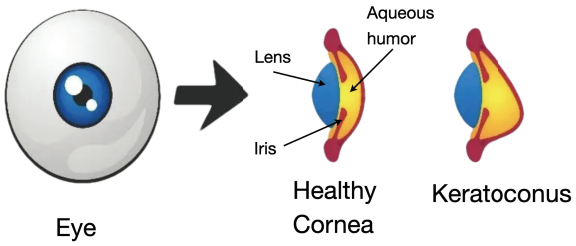

Figure 3. Shapes of a normal cornea, left, compared with that of a cornea affected by keratoconus.

but there is evidence about a specific role also played by other genes. We are far from understanding the exact genetic malfunctioning leading to the disease: some further hints about its onset mechanisms may be given by the observation that keratoconus is correlated with some atopic diseases like asthma, allergies, and eczema and that it is very frequent that several or all of these diseases affect the same person simultaneously. According to the available evidence [8], the most important risk factors for keratoconus are a family history of keratoconus, allergy, asthma, mechanical stress such as eye rubbing or eyelids extra-pressure, and eczema.

What is certain is that patients with a parent, sibling, or child who has keratoconus have 15 to 67 times higher risk of developing corneal ectasia (i.e., a change in the corneal curvature leading to impairing optical defects) compared to patients with no affected relatives: Keratoconus surely affects about 1 in 2000 people, but some estimates suggest that its incidence may be as high as 1 in 400 individuals.[1]

In Figure 3, the typical shape of a cornea affected by keratoconus is shown, while in Figure 4, the digital reconstruction of typical outer shapes of healthy and keratoconus affected corneal tissues is shown. The reader will observe that the "drop-like" shape of keratoconus-affected corneas shows a "lower" bulge: one of the theses put forward in the present paper is that this shape is driven by multiple factors. The numerical analysis presented in this paper indicates that, among the considered deformation mechanisms, probably the most dominant one is related to two main factors: specifically, the uniform damage of keratoconus corneas and the mechanical effects of the eyelids on the deformation shapes of the corneas. Indeed, as corneas are living tissues, the presence of external interacting forces, after the degeneration of mechanical properties, permanently changes the keratoconus cornea shape, with detrimental optical effects. The situation is even worse in the presence of transplanted corneas whose mechanical properties are highly inhomogeneous: the donor cornea is essentially healthy, while the residual patient corneal tissue remains affected by keratoconus and shows much weaker mechanical stiffness. In conclusion, we claim that (1) it is logically more economical to assume that keratoconus shapes are the consequence of a uniform degeneration of cornea and of the effects of interaction with eyelids, and (2) cornea transplants must also be designed taking into account the mechanical properties of the residual patient corneal tissue.

In Figure 5, a representative contour plot of corneal curvatures in corneas affected by keratoconus is shown.

In Figure 6, it is shown the shape of a transplanted cornea with severe residual astigmatism (on the left) and the contour plot of calculated sagittal curvature (on the right). It has to be remarked that the penetrating keratoplasty technique used in the presented case used a selective removal of suture stitches, which aimed at obtaining the observed nearly vertical pattern of concentrated curvature. This technique allowed for an optical correction using eyeglasses, albeit with very high diopters (19 for equivalent astigmatism and 5 for equivalent hypermetropia).

In Figure 7, the elaborated images were obtained by digital elaboration of several pictures of a transplanted cornea. Its final shape and curvature appear to be highly irregular: the digital image correlation, on which the used image reconstruction software (i.e., OCULUS Pentacam®) is based, does not manage to give a result. In the considered clinical case, the penetrating keratoplasty was followed by an initial event of rejection, blocked with heavy anti-rejection treatment. Indeed, the corneal tissue degeneration, which was caused by the rejection initiation and by the following corneal degeneration, made the shape so irregular that the available digital recognition techniques failed in producing the whole surface rendering.[2]

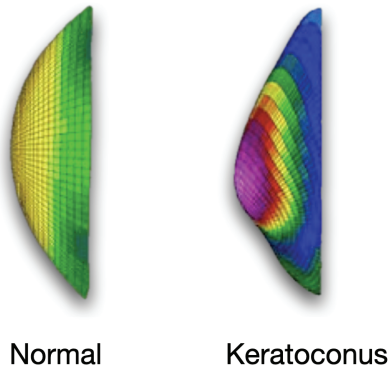

Figure 4. Digital reconstruction of the surface of a normal cornea, left, compared with that of a cornea affected by keratoconus.

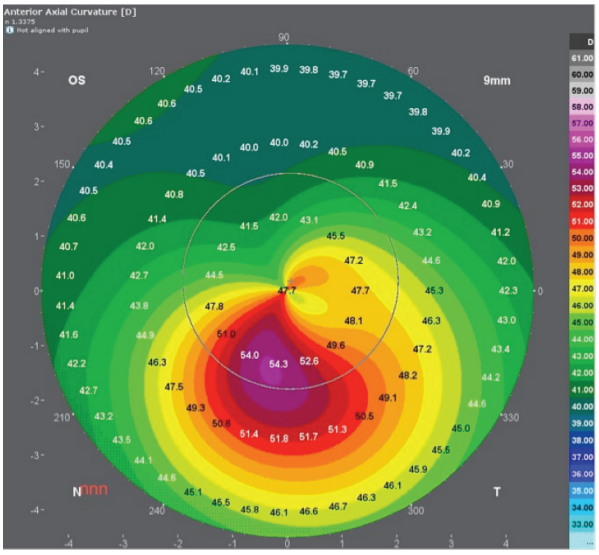

Figure 5. Contour plot of curvature field in a cornea affected by keratoconus.

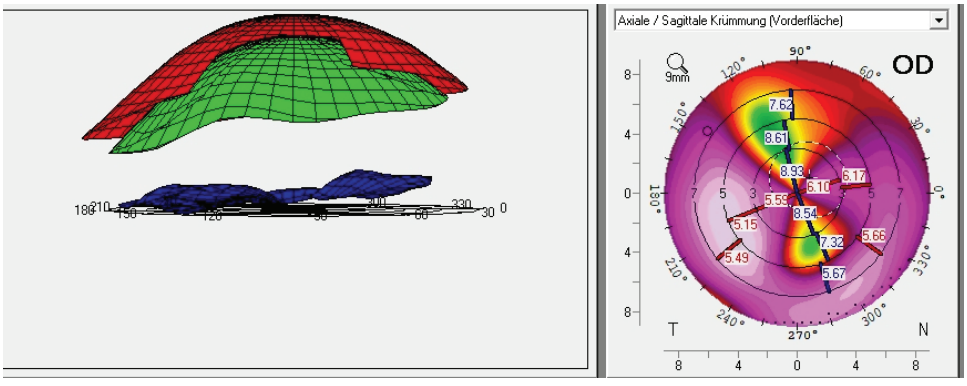

Figure 6. Digital elaboration of several images of a transplanted cornea with severe residual astigmatism (19 diopters).

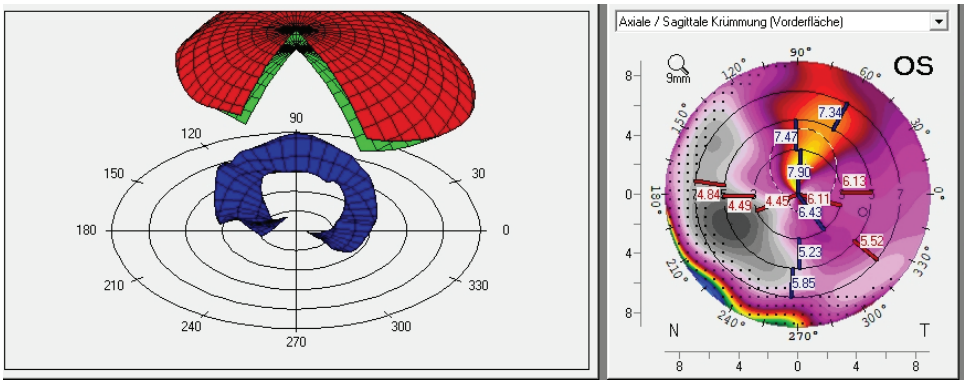

Figure 7. Digital elaboration of a transplanted cornea with extremely irregular shape and curvature.

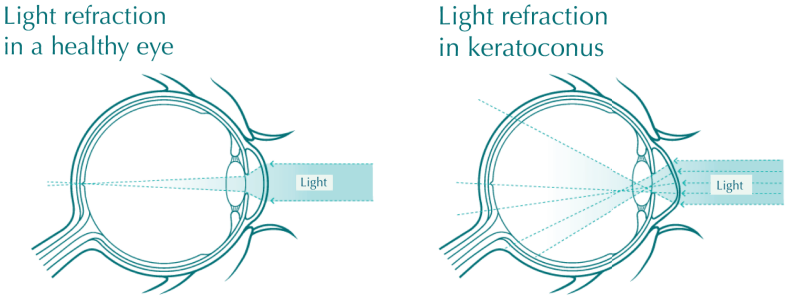

Figure 8. What occurs when light rays are multiply and irregularly diffracted by corneas affected by keratoconus.

It is also believed that keratoconus is related to some malfunctioning of the physiological corneal regeneration process, which mainly occurs in its epithelium layer. The models developed for describing the mechanical behaviour of self-regenerating tissues [9–11] must be adapted to the case of corneal epithelium, to determine the impact of this possible etiological cause of the disappearance of Bowman's layer and the consequent keratoconus degeneration.

1.3. The effects of keratoconus on vision

A cornea affected by keratoconus is not behaving as it should: i.e., as a lens converging and focusing images on the retina (see Figure 8).

Keratoconus, in an advanced stage, results in (1) blurry vision, (2) double or multiple vision, (3) nearsightedness, (4) very irregular astigmatism, and (5) light sensitivity. All these symptoms may lead to a very poor quality of life; in fact, usually, both eyes are affected. In the most severe cases, a scarring or a circle may be seen within the cornea.

In Figure 9, we can see a reconstruction of the multiple images seen by a person with keratoconus. For instance, as observed already by Nottingham [1] in 1854: "a candle appears like a big number of lights, confusedly running into one another, one letter is blurred by several of its images surrounding and superimposed on it."

This pattern is highly variable from case to case and often takes on new forms for the same patient, sometimes even on a daily basis: some patients may commonly notice streaking and flaring distortion around light sources, and some others even notice that the images are moving relatively to one another in time, in a synchronous way with their heartbeat.

These optical effects can be explained by some histological observations of the corneal-stroma structural changes that are observed in corneal tissue affected by keratoconus. In Figure 10, it is schematically shown the result of a typical histopathology exam of such a tissue: even in the presence of corneal-stroma

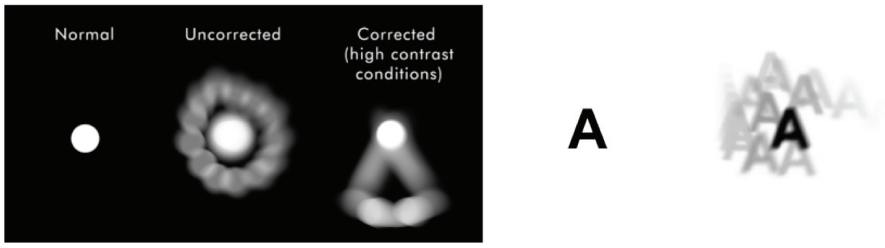

Figure 9. What one sees through a cornea affected by keratoconus.

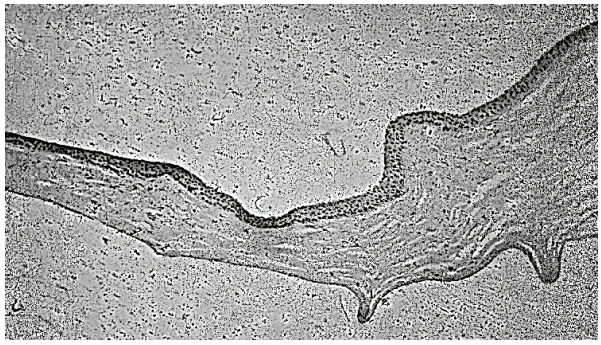

Figure 10. A typical histopathology exam of corneal stroma affected by keratoconus.

moderate thinning, some wrinkles of the posterior and anterior surfaces are observed: their effect on light refraction is the ultimate cause of sight impairing (in this context, we cite Cogan [12] for its beautiful early results).

1.4. The aim of the present paper

The aim of this paper is to develop and analyse a 2D reduced-order generalised continuum model that can move in a 3D space. We want to apply it to the study of the biomechanical behaviour of corneas affected by keratoconus before and after penetrating keratoplasty. The model is derived from a 3D continuum theory by applying a micro-macro kinematical map, simplifying the corneal structure while continuing to account for the essential mechanical properties of the considered system. By incorporating variations in material properties due to pathological degeneration and surgical intervention, the study seeks to provide insights into the deformation mechanisms that lead to characteristic shape changes in keratoconus-affected and transplanted corneas. Furthermore, the paper explores the mechanical agents that, together with internal ocular pressure, reshape keratoconus-affected corneas before and after transplants, offering a multi-factorial explanation for the asymmetric bulging observed in keratoconus patients. Our results contribute to a more detailed description of corneal mechanics, with implications for improving surgical outcomes and developing more effective treatment strategies for corneal pathologies.

2. Formulation of the used 3D Cauchy continuum model

We model, at the micro-level, the cornea as a 3D Cauchy continuum whose deformation energy depends quadratically on the Cauchy–Green non-linear deformation measure C. However, such a 3D model is too detailed and cannot be easily used to explore the consequences of our modelling assumptions because of the computational burden implied in a long series of parametric simulations. To get a more viable model, we will use a reduction order procedure, producing a generalised 2D continuum model,[3] in which at least the additional kinematical parameter "thickness" of the corneal is added to the standard kinematical parameters used in the theory of shells. This procedure is of the same kind as those introduced by Eremeyev et al. [13–17].

2.1. Kinematics and deformation measures

The placement field $\mathbf{\Pi}$ is defined in the reference domain $D \times [-l_0/2, l_0/2]$. In formulas:

$$\mathbf{\Pi} : D \times [-l_0/2, l_0/2] \to \mathscr{E}^3 \tag{1}$$

where the plane region $D \subset \mathbb{R}^2$ will be assumed to be elliptical, $\mathscr{E}^3$ is the Euclidean 3D space of positions and l_0 denotes the cornea reference thickness. A generic point $\boldsymbol{X}$ in the reference domain $D \times [-l_0/2, l_0/2]$ is, therefore, determined by the two coordinates X^α ($\alpha = 1, 2$) spanning in the plane region D and a third coordinate $X^3 \in [-l_0/2, l_0/2]$; when necessary, we will denote $\{\boldsymbol{E}_\alpha, \boldsymbol{E}_3\}$ the vector basis in the reference configuration.

If $T\mathscr{E}^3$ denotes the vector space of the translations in $\mathscr{E}^3$ and $\{\boldsymbol{e}_i\}$, $i = 1, 2, 3$, is a basis in it, we can introduce the coordinates representation

$$\mathbf{\Pi}(\boldsymbol{X}) = \Pi^i(X^\alpha, X^3)\boldsymbol{e}_i. \tag{2}$$

By introducing the placement gradient:

$$\boldsymbol{F} := \nabla \mathbf{\Pi}; \quad F^i_J = \frac{\partial \Pi^i}{\partial X^J} \tag{3}$$

where we adopt the notation employing lowercase letters for spatial coordinates and capital letters for material coordinates, the Cauchy–Green deformation measure $\boldsymbol{C}$ is given by

$$\boldsymbol{C} := \boldsymbol{F}^\top \boldsymbol{F}; \quad C^L_M = F^L_i F^i_M. \tag{4}$$

where the superscript $\top$ denotes the transposition of a tensor.

The Green–Saint Venant tensor is given by

$$2\boldsymbol{G} := \boldsymbol{F}^\top \boldsymbol{F} - \boldsymbol{I} \tag{5}$$

where $\boldsymbol{I}$ is the identity tensor in the reference configuration.

In this paper, we will not try to introduce higher gradient continuum models at the "micro" level at which the cornea shape is modelled as a subset of Euclidean space having non-vanishing volume, i.e., by means of higher gradient continuum models. When this effort will be attempted, then the deformation measures have to include those listed in works by Auffray et al. [18] and dell'Isola et al. [19], Dell'Isola et al. [20]: i.e., all the needed Lagrangian gradients of $\boldsymbol{G}$.

2.2. Deformation energy functional

The most general first-gradient deformation energy functional, which can be introduced for the considered 3D Cauchy continuum, has the following form:

$$\mathcal{E}_V{}^{\text{def}} := \int_{D \times [-l_0/2, l_0/2]} \mathfrak{e}_V{}^{\text{def}}(\boldsymbol{G}, \boldsymbol{X}) \, \mathrm{d}V \tag{6}$$

where $\mathfrak{e}_V{}^{def}$ represents the volume density of deformation energy in the material point $\boldsymbol{X}$ and $\mathrm{d}V$ is the volume measure in the reference configuration.

We will limit ourselves (albeit we are aware of the fact that this assumption is very limiting, see e.g., Pandolfi and Holzapfel [2], Pandolfi and Manganiello [3], Pandolfi and Vasta [4], so that in future investigations we will be obliged to generalise it) to use a volume density of deformation energy that is quadratic in the non-linear deformation measure $\boldsymbol{G}$. In formulas:

$$\mathfrak{e}_V{}^{\text{def}} = \frac{1}{2} G^L_M G^H_K \mathbb{C}^{MK}_{LH}. \tag{7}$$

For our modelling purposes, the stiffness tensor $\mathbb{C}$ must depend on the material particle $\boldsymbol{X}$: in fact, we will model the mechanical damage, which is induced by the pathogenic process causing keratoconus, by assuming that the values of one or more among the stiffness parameters in the tensor $\mathbb{C}$ decrease, in some cases even non-uniformly, in the variables $\boldsymbol{X}$.[4]

In the present paper, specifically, we consider a heterogeneous compliance tensor $\mathbb{S}$, which is related to the usual engineering constants for orthotropic materials [21] and using Voigt notation, as given by the formulas:

$$\begin{aligned} &\mathbb{S}_{11} = \tfrac{1}{Y_1}, && \mathbb{S}_{22} = \tfrac{1}{Y_2}, && \mathbb{S}_{33} = \tfrac{1}{Y_3}, \\ &\mathbb{S}_{12} = \tfrac{-\nu_{12}}{Y_1}, && \mathbb{S}_{13} = \tfrac{-\nu_{13}}{Y_1}, && \mathbb{S}_{23} = \tfrac{-\nu_{23}}{Y_2}, \\ &\mathbb{S}_{44} = \tfrac{1}{2\mu_{23}}, && \mathbb{S}_{55} = \tfrac{1}{2\mu_{13}}, && \mathbb{S}_{66} = \tfrac{1}{2\mu_{12}}, \end{aligned} \tag{8}$$

where Young's moduli in the directions of orthotropy are Y_1, Y_2, Y_3; Poisson's ratios are ν_{12}, ν_{13}, ν_{23}; and the shear moduli are μ_{12}, μ_{13}, μ_{23}. The stiffness tensor $\mathbb{C}$ is evaluated from the inverse of the matrix representation of $\mathbb{S}$.

To better describe the properties of physiological or degenerated corneas, we will assume that the region D can be partitioned into several regions (see again Pandolfi and Holzapfel [2], Pandolfi and Manganiello [3], Pandolfi and Vasta [4], De Bellis et al. [22, 23], Pandolfi et al. [24, 25]), in each of which the stiffness parameters have some specific values, modelling the fibrous structure of the cornea: they are shown in Figure 11.[5] Specifically, the elastic moduli, including the Young moduli and shear moduli, are normalised using a characteristic value of the Young modulus for corneal tissue, which is established at 0.2 MPa [26,27].

The two central bands forming the cross exhibit pronounced stiffness, vertically in the vertical band and horizontally in the horizontal band, while within the residual lobes, the stiffness tensor is predominantly transversally isotropic, characterised by a symmetry axis directed along the thickness of the cornea. The material properties were assigned with particular attention to the lamellar structure of collagen fibrils, which are known, from a macroscopic point of view, to be arranged following the pattern shown in Figure 11 to provide corneal strength and stability.

2.3. External work functional

The previously introduced deformation energy functional form implies that, in the framework of the introduced model, the following particular external work functional can be sustained:

$$\delta\mathcal{W}^{\text{ext}} = \int\limits_{D\times\{-l_0/2\}} (-\mathrm{p}\,\boldsymbol{n}\cdot\delta\boldsymbol{\Pi})\,\mathrm{J}_A\mathrm{d}A_D + \int\limits_{D\times[-l_0/2,l_0/2]} (-\rho^*\boldsymbol{g}\cdot\delta\boldsymbol{\Pi})\,\mathrm{d}V \tag{9}$$

where

- the ρ^* and $\boldsymbol{g}$ denote, respectively, the reference volume mass density and the gravity acceleration;
- the pressure p will be assumed to be constant in space;
- $\delta\boldsymbol{\Pi}$ is the virtual variation of placement;
- $\mathrm{d}A_D$ and $\mathrm{d}V$ are, respectively, the area and volume measures of the domain D in the reference configuration;
- $\boldsymbol{n}$ is the current normal to the surface $\boldsymbol{\Pi}\,(D\times\{-l_0/2\})$; and
- J_A represents the change of area density from reference to actual configuration. These last two are given by well-known Piola formulas [28]:

$$\boldsymbol{n} = \frac{\boldsymbol{F}^{-\top}\boldsymbol{N}}{\left\|\boldsymbol{F}^{-\top}\boldsymbol{N}\right\|}, \quad \mathrm{J}_A = \left\|\boldsymbol{F}^{-\top}\boldsymbol{N}\right\| \det\boldsymbol{F}. \tag{10}$$

in terms of the placement gradient and the reference unit normal $\boldsymbol{N}$.

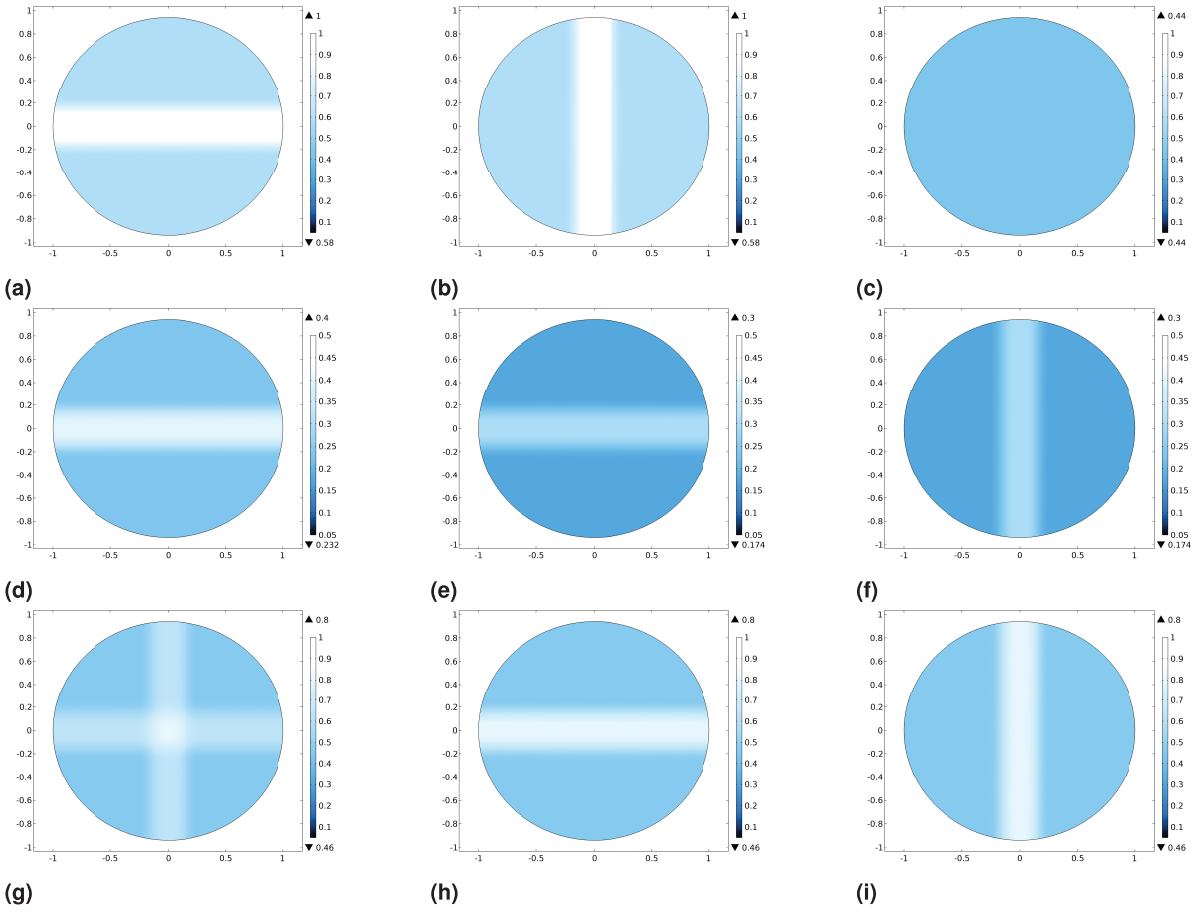

Figure 11. Dimensionless engineering constants for orthotropic materials: (a) elastic modulus Y_1, (b) elastic modulus Y_2, (c) elastic modulus Y_3, (d) Poisson ratio ν_{12}, (e) Poisson ratio ν_{13}, (f) Poisson ratio ν_{23}, (g) shear modulus μ_{12}, (h) shear modulus μ_{13}, (i) shear modulus μ_{23}.

3. Reduction to a 2D generalised continuum model

In order to describe the damage-induced changes of shape in corneas, using a model whose prediction can be obtained with relatively lower computational complexity, we prefer to use a 2D continuum model. However, as the thickness of the cornea plays a relevant role in the phenomena whose prediction we are interested in, the kinematics to be introduced must be enriched with respect to the one used in standard shell theory. Therefore, together with the *mean surface* placement field $\mathbf{\Pi}_R$, as a further kinematical descriptor, the additional vector field $\boldsymbol{d}$ describing the current cornea thickness is considered to complete the set of kinematical descriptors to be used in the reduced-order 2D model. A micro-macro kinematical map will be used to postulate a form of 3D placement in terms of the 2D kinematical descriptors: the *Ansatz* which we accept here is fully justified by the physiological ratio between the corneal thickness and diameter (≈ 0.04) and by the kind of applied loads to which consideration is limited.

3.1. 2D kinematics and micro-macro kinematical map

The micro-macro kinematical map, which we assume, gives the 3D placement introduced in equation (1) by means of the following formula:

$$\mathbf{\Pi}(X^\alpha, X^3) = \mathbf{\Pi}_R(X^\alpha) + X^3 \boldsymbol{d}(X^\alpha) \tag{11}$$

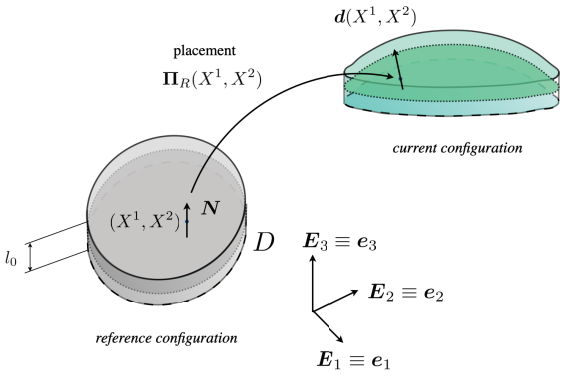

Figure 12. Sketch of the kinematical maps.

where

$$\boldsymbol{\Pi}_R : D \to \mathscr{E}^3; \quad \boldsymbol{d} : D \to T\mathscr{E}^3 \tag{12}$$

are, respectively, the *mean surface* placement and the *corneal thickness* vector fields (see Figure 12). We note that the newly introduced field $\boldsymbol{d}$ represents the image of the mean surface normal unit vector through the map $\boldsymbol{\Pi}$. This vector field is not constrained to remaining normal to the current mean surface, nor is it required to remain a unit vector.

Moreover, we assume that

$$\mathbb{C}(\boldsymbol{X}) = \mathbb{C}_0(X^\alpha) + X^3\,\mathbb{C}_1(X^\alpha)\ . \tag{13}$$

The hypothesis that assumes linear dependence in X^3 represents the simplest explanation for the mechanical inhomogeneity observed in keratoconus corneas (see Pandolfi and Holzapfel [2]). Nonetheless, the numerical analyses conducted herein indicate the necessity to extend this hypothesis by incorporating a more complex dependence on X^3.

Using equation (11), we can calculate the corresponding 3D deformation gradient

$$\boldsymbol{F} = \frac{\partial \boldsymbol{\Pi}_R}{\partial X^\alpha} \otimes \boldsymbol{E}^\alpha + X^3 \frac{\partial \boldsymbol{d}}{\partial X^\alpha} \otimes \boldsymbol{E}^\alpha + \boldsymbol{d} \otimes \boldsymbol{E}^3 = \nabla_R \boldsymbol{\Pi}_R + X^3 \nabla_R \boldsymbol{d} + \boldsymbol{d} \otimes \boldsymbol{E}^3 \tag{14}$$

and its transpose

$$\boldsymbol{F}^\top = \boldsymbol{E}^\alpha \otimes \frac{\partial \boldsymbol{\Pi}_R}{\partial X^\alpha} + X^3 \boldsymbol{E}^\alpha \otimes \frac{\partial \boldsymbol{d}}{\partial X^\alpha} + \boldsymbol{E}^3 \otimes \boldsymbol{d} = (\nabla_R \boldsymbol{\Pi}_R)^\top + X^3 (\nabla_R \boldsymbol{d})^\top + \boldsymbol{E}^3 \otimes \boldsymbol{d} \tag{15}$$

where we have introduced the notation

$$\nabla_R := \frac{\partial}{\partial X^\alpha} \otimes \boldsymbol{E}^\alpha. \tag{16}$$

In this way, we arrive to represent the 3D Cauchy–Green tensor as follows

$$\begin{aligned} \boldsymbol{C} = \boldsymbol{F}^\top \boldsymbol{F} = \boldsymbol{C}_R + X^3 \operatorname{tr}(\boldsymbol{F}_R \otimes \nabla_R \boldsymbol{d} + \nabla_R \boldsymbol{d} \otimes \boldsymbol{F}_R) + \\ + \left(X^3\right)^2 \operatorname{tr}(\nabla_R \boldsymbol{d} \otimes \nabla_R \boldsymbol{d}) + \boldsymbol{F}_R^\top \boldsymbol{d} \otimes \boldsymbol{E}^3 + \boldsymbol{E}^3 \otimes \boldsymbol{F}_R^\top \boldsymbol{d} + \\ + \frac{1}{2}\left(\nabla_R \|\boldsymbol{d}\|^2 \otimes \boldsymbol{E}^3 + \boldsymbol{E}^3 \otimes \nabla_R \|\boldsymbol{d}\|^2\right) + \|\boldsymbol{d}\|^2 \boldsymbol{E}^3 \otimes \boldsymbol{E}^3 \end{aligned} \tag{17}$$

where the tensor product is to be considered with respect to the reference vector space and the trace, $\operatorname{tr}(\cdot)$, with respect to the current vector space; in formulas, if g_{ij} denotes the inner product in the current

configuration and

$$\begin{aligned} \operatorname{tr}\left(\boldsymbol{F}_R \otimes \nabla_R \boldsymbol{d} + \nabla_R \boldsymbol{d} \otimes \boldsymbol{F}_R\right) &= g_{ij}\left(\frac{\partial \Pi_R^i}{\partial X^\alpha}\frac{\partial d^j}{\partial X^\beta} + \frac{\partial \Pi_R^i}{\partial X^\beta}\frac{\partial d^j}{\partial X^\alpha}\right)\boldsymbol{E}^\beta \otimes \boldsymbol{E}^\alpha \\ \operatorname{tr}\left(\nabla_R \boldsymbol{d} \otimes \nabla_R \boldsymbol{d}\right) &= g_{ij}\left(\frac{\partial d^i}{\partial X^\alpha}\frac{\partial d^j}{\partial X^\beta}\right)\boldsymbol{E}^\beta \otimes \boldsymbol{E}^\alpha \end{aligned} \tag{18}$$

Moreover, we have used the notations:

$$\begin{aligned} &\boldsymbol{F}_R := \nabla_R \boldsymbol{\Pi}_R; && (F_R)^i_\alpha = \frac{\partial \Pi_R^i}{\partial X^\alpha} \\ &\boldsymbol{C}_R := \boldsymbol{F}_R^\top \boldsymbol{F}_R; && (C_R)^\beta_\alpha = (F_R)^\beta_i\,(F_R)^i_\alpha \\ &\boldsymbol{F}_R^\top \boldsymbol{d}; && \left(F_R^\top d\right)^\beta = (F_R)^\beta_i\, d^i. \end{aligned} \tag{19}$$

Therefore, in the introduced reduced-order model, the (objective) deformation measures are as follows:

$$\begin{gathered} \nabla_R \|\boldsymbol{d}\|^2\,; \quad \boldsymbol{F}_R^\top \boldsymbol{d}\,; \quad \boldsymbol{C}_R\,; \quad \|\boldsymbol{d}\|^2 \\ \operatorname{tr}\left(\nabla_R \boldsymbol{d} \otimes \nabla_R \boldsymbol{d}\right) \\ \operatorname{tr}\left(\boldsymbol{F}_R \otimes \nabla_R \boldsymbol{d} + \nabla_R \boldsymbol{d} \otimes \boldsymbol{F}_R\right) \end{gathered} \tag{20}$$

The Green–Saint-Venant tensor is, therefore, given by

$$\begin{aligned} 2\boldsymbol{G} = \boldsymbol{F}^\top \boldsymbol{F} - \boldsymbol{I} = 2\boldsymbol{G}_R + X^3 \operatorname{tr}\left(\boldsymbol{F}_R \otimes \nabla_R \boldsymbol{d} + \nabla_R \boldsymbol{d} \otimes \boldsymbol{F}_R\right) + \\ + \left(X^3\right)^2 \operatorname{tr}\left(\nabla_R \boldsymbol{d} \otimes \nabla_R \boldsymbol{d}\right) + \boldsymbol{F}_R^\top \boldsymbol{d} \otimes \boldsymbol{E}^3 + \boldsymbol{E}^3 \otimes \boldsymbol{F}_R^\top \boldsymbol{d} + \\ + \frac{1}{2}\left(\nabla_R \|\boldsymbol{d}\|^2 \otimes \boldsymbol{E}^3 + \boldsymbol{E}^3 \otimes \nabla_R \|\boldsymbol{d}\|^2\right) + \left(\|\boldsymbol{d}\|^2 - 1\right)\boldsymbol{E}^3 \otimes \boldsymbol{E}^3 \end{aligned} \tag{21}$$

where we have used the decomposition of the identity

$$\boldsymbol{I} = \boldsymbol{E}^\alpha \otimes \boldsymbol{E}_\alpha + \boldsymbol{E}^3 \otimes \boldsymbol{E}_3 =: \boldsymbol{I}_R + \boldsymbol{E}^3 \otimes \boldsymbol{E}_3 \tag{22}$$

and the notation

$$2\boldsymbol{G}_R = \boldsymbol{C}_R - \boldsymbol{I}_R. \tag{23}$$

The shown micro-macro kinematical map can be generalised in various ways: for instance, by assuming a different dependence on X^3 (possibly a higher order polynomial or a suitably chosen other function) Dell'Isola and Kosinski [29] or explicitly introducing in it the gradient of placement or the gradient of thickness, in order to account, at macro-level, for the energies related to the high gradients, at micro-level, of micro-placement or of micro-stiffness [30–32]. An interesting effort for getting a micro-macro identification for a 3D continuum model starting from a discrete microscopic truss model is made in the work by Köry et al. [33]. We remark that the large shape and asymmetric variations occurring in keratoconus corneas before and after penetrating keratoplasty cannot be shown in the just cited paper, as both the micro-macro identification and the study of the corneal deformation are made in the cylindrical symmetry case. Therefore, herein, we present both a 2D and a 3D continuum model in which general 3D displacements and deformations can occur. We emphasise that it is essential, in the study of the keratoconus, to take into account both corneal anisotropy and inhomogeneity.

3.2. 2D deformation energy functional

The most general first gradient deformation energy functional, which can be introduced for considered 2D generalised continua, has the following form:

$$\mathcal{E}_S{}^{\mathrm{def}} := \int_D \mathfrak{e}_S{}^{\mathrm{def}} \left(\nabla_R \|\boldsymbol{d}\|^2 ; \boldsymbol{F}_R^T \boldsymbol{d}; \boldsymbol{C}_R; \|\boldsymbol{d}\|^2 ; \mathrm{tr}\left(\nabla_R \boldsymbol{d} \otimes \nabla_R \boldsymbol{d}\right) ; \mathrm{tr}\left(\boldsymbol{F}_R \otimes \nabla_R \boldsymbol{d} + \nabla_R \boldsymbol{d} \otimes \boldsymbol{F}_R\right) ; \boldsymbol{X}_R \right) \mathrm{d}A_D \quad (24)$$

where $\mathfrak{e}_S{}^{\mathrm{def}}$ represents the surface density of deformation energy in the material point $\boldsymbol{X}_R \in D$ given by the coordinates X^α and $\mathrm{d}A_D$ is the surface measure in the reference configuration.

The micro-macro kinematical map allows for an identification of a form of $\mathfrak{e}_S{}^{\mathrm{def}}$ in terms of the stiffness tensor field $\mathbb{C}(\boldsymbol{X})$ by imposing the equality of $\mathcal{E}_S{}^{\mathrm{def}}$ with $\mathcal{E}_V{}^{\mathrm{def}}$.

In fact,

$$\mathfrak{e}_S{}^{\mathrm{def}}\left(X^\alpha\right) = \int_{-l_0/2}^{+l_0/2} \mathfrak{e}_{\mathrm{V}}{}^{\mathrm{def}}\left(\boldsymbol{G}, X^\alpha, X^3\right) \mathrm{d}X^3. \quad (25)$$

As we have assumed equation (7), we have

$$\mathfrak{e}_S{}^{\mathrm{def}}\left(X^\alpha\right) = \int_{-l_0/2}^{+l_0/2} \frac{1}{2} G_M^L(X^\alpha, X^3) G_K^H(X^\alpha, X^3) \mathbb{C}_{LH}^{MK}\left(X^\alpha, X^3\right) \mathrm{d}X^3. \quad (26)$$

The explicit form of $\mathfrak{e}_S{}^{\mathrm{def}}$ can be, then, simply obtained by replacing in the last equation the reduction formula (21) and (13).

In the present paper, we find equilibrium configurations for keratoconus cornea and transplanted corneas by minimising the just postulated deformation and total energy. The kinematical parameters to be chosen for this minimisation are the displacement $\boldsymbol{u}(X^\alpha) = \boldsymbol{\Pi}_R - \boldsymbol{X}_R$ of the reference domain D, which characterises the middle surface, and the variable $\boldsymbol{d}(X^\alpha)$, which accounts for the influence of thickness changes. In the present treatment, finding the strong form of the equilibrium equation, i.e., the governing PDE with corresponding natural boundary conditions, is not required because we will immediately use a numerical integration scheme based on finite element minimisation techniques and essential boundary conditions.

Specifically, to clarify the weak form of the governing equation, we introduce the following notation:

$$\boldsymbol{A} = \mathrm{tr}\left(\boldsymbol{F}_R \otimes \nabla_R \boldsymbol{d} + \nabla_R \boldsymbol{d} \otimes \boldsymbol{F}_R\right), \quad (27)$$

$$\boldsymbol{H} = \mathrm{tr}\left(\nabla_R \boldsymbol{d} \otimes \nabla_R \boldsymbol{d}\right), \quad (28)$$

$$\boldsymbol{Q} = \boldsymbol{F}_R^\top \boldsymbol{d} \otimes \boldsymbol{E}^3 + \boldsymbol{E}^3 \otimes \boldsymbol{F}_R^\top \boldsymbol{d} + \frac{1}{2}\left(\nabla_R \|\boldsymbol{d}\|^2 \otimes \boldsymbol{E}^3 + \boldsymbol{E}^3 \otimes \nabla_R \|\boldsymbol{d}\|^2\right) + \left(\|\boldsymbol{d}\|^2 - 1\right) \boldsymbol{E}^3 \otimes \boldsymbol{E}^3 \quad (29)$$

which simplifies the Green–Saint-Venant tensor as below:

$$2\boldsymbol{G} = 2\boldsymbol{G}_R + X^3 \boldsymbol{A} + \left(X^3\right)^2 \boldsymbol{H} + \boldsymbol{Q}. \quad (30)$$

By substituting equations (30) and (13) into equation (26) and integrating over X^3-variable, the surface density of deformation energy becomes:

$$\mathfrak{e}_S{}^{\mathrm{def}} = \frac{l_0}{2} \left(\boldsymbol{G}_R \mathbb{C}_0 \boldsymbol{G}_R + \frac{1}{2} \boldsymbol{G}_R \mathbb{C}_0 \boldsymbol{Q} + \frac{1}{2} \boldsymbol{Q} \mathbb{C}_0 \boldsymbol{G}_R + \frac{1}{4} \boldsymbol{Q} \mathbb{C}_0 \boldsymbol{Q} \right) +$$

$$+\frac{{l_0}^3}{24}\left(\frac{1}{2}\boldsymbol{G}_R\mathbb{C}_0\boldsymbol{H}+\frac{1}{2}\boldsymbol{H}\mathbb{C}_0\boldsymbol{G}_R+\frac{1}{4}\boldsymbol{A}\mathbb{C}_0\boldsymbol{A}+\frac{1}{4}\boldsymbol{H}\mathbb{C}_0\boldsymbol{Q}+\frac{1}{4}\boldsymbol{Q}\mathbb{C}_0\boldsymbol{H}+\right.$$
$$\left.+\frac{1}{2}\boldsymbol{G}_R\mathbb{C}_1\boldsymbol{A}+\frac{1}{2}\boldsymbol{A}\mathbb{C}_1\boldsymbol{G}_R+\frac{1}{4}\boldsymbol{A}\mathbb{C}_1\boldsymbol{Q}+\frac{1}{4}\boldsymbol{Q}\mathbb{C}_1\boldsymbol{A}\right)+\frac{{l_0}^5}{160}\left(\frac{1}{4}\boldsymbol{H}\mathbb{C}_0\boldsymbol{H}+\frac{1}{4}\boldsymbol{A}\mathbb{C}_1\boldsymbol{H}+\frac{1}{4}\boldsymbol{H}\mathbb{C}_1\boldsymbol{A}\right). \quad (31)$$

The corresponding expression for the 2D deformation energy ${\mathcal{E}_S}^{\mathrm{def}}$ (as defined in equation (24)), therefore, by using only two-dimensional fields, incorporates some 3D deformation effects based on the assumed linear dependence of the 3D placement Π.

By applying the same methodology to the external work functional (9), and incorporating therein the kinematical simplifying assumption (11), results in the derivation of the reduced form of external virtual work, which is expressed as follows:

$$\delta\mathcal{W}_R^{\mathrm{ext}}=\int\limits_{D\times\{-l_0/2\}}(-\mathrm{p}\,\boldsymbol{n}\cdot\delta\boldsymbol{\Pi})\,\mathrm{J}_A\mathrm{d}A_D+\int\limits_D\left(-\rho_A^*\,\boldsymbol{g}\cdot\delta\boldsymbol{u}\right)\mathrm{d}A_D \quad (32)$$

where ρ_A^* represents the mass density per unit of area of the cornea.

Therefore, the two-dimensional governing equation of the cornea can be explicitly expressed using directly equations (31) and (32) as follows:

$$\delta{\mathcal{E}_S}^{\mathrm{def}}-\delta\mathcal{W}_R^{\mathrm{ext}}=0\,. \quad (33)$$

3.3. Boundary conditions in 2D generalised continuum model

The essential boundary conditions, which can be imposed in every point in ∂D, are

$$\begin{aligned}\forall X^\alpha\in D\qquad &\boldsymbol{\Pi}_R(X^\alpha)=\boldsymbol{X}_R+\boldsymbol{U}_0(X^\alpha)\\ \forall X^\alpha\in D\qquad &\boldsymbol{d}(X^\alpha)=\boldsymbol{N}+\boldsymbol{v}_0(X^\alpha)\end{aligned} \quad (34)$$

where the fields $\boldsymbol{U}_0$ and $\boldsymbol{v}_0$ are assigned boundary displacements and thickness variations, respectively.

The integration by parts of the energy functional given in equation (24) can give the corresponding natural boundary conditions. In the present work, we start our analysis based on essential boundary conditions only: more detailed modelling of the mechanical connection between the cornea, the sclera and the other structural elements of the *bulbus oculi* will necessarily require this further modelling analysis.[6]

4. Calculation of deformed shapes with varying values of the externally applied uniform pressure

In order to evaluate the predictive capabilities of the proposed reduced model, we conducted numerical simulations utilising the finite element method. We implemented a numerical code based on the proposed model within the commercial software Comsol Multiphysics. This software allows us to perform finite element analysis in a weak formulation using directly equation (33).

In the numerical simulation, we use a dimensionless form for the problem at hand since it simplifies analysis, enhances the understanding of underlying phenomena, and allows for more efficient and accurate solutions. This non-dimensional representation of the problem is achieved by normalising the lengths relative to the characteristic length L_0, specifically referring to the major semi-axis of the cornea in the horizontal direction, which is assumed to be 5.5 mm. The elastic moduli, encompassing both Young's and shear moduli, are normalised with respect to the characteristic Young modulus of the cornea, denoted as Y_0, established at 0.2 MPa. The intraocular pressure (IOP), which denotes the fluid pressure exerted within the eye and consequently on the cornea, is within the range of 10–20 mmHg (equivalent to 1.333–2.666 kPa) [34] and is similarly normalised by the characteristic Young modulus Y_0, as is the specific

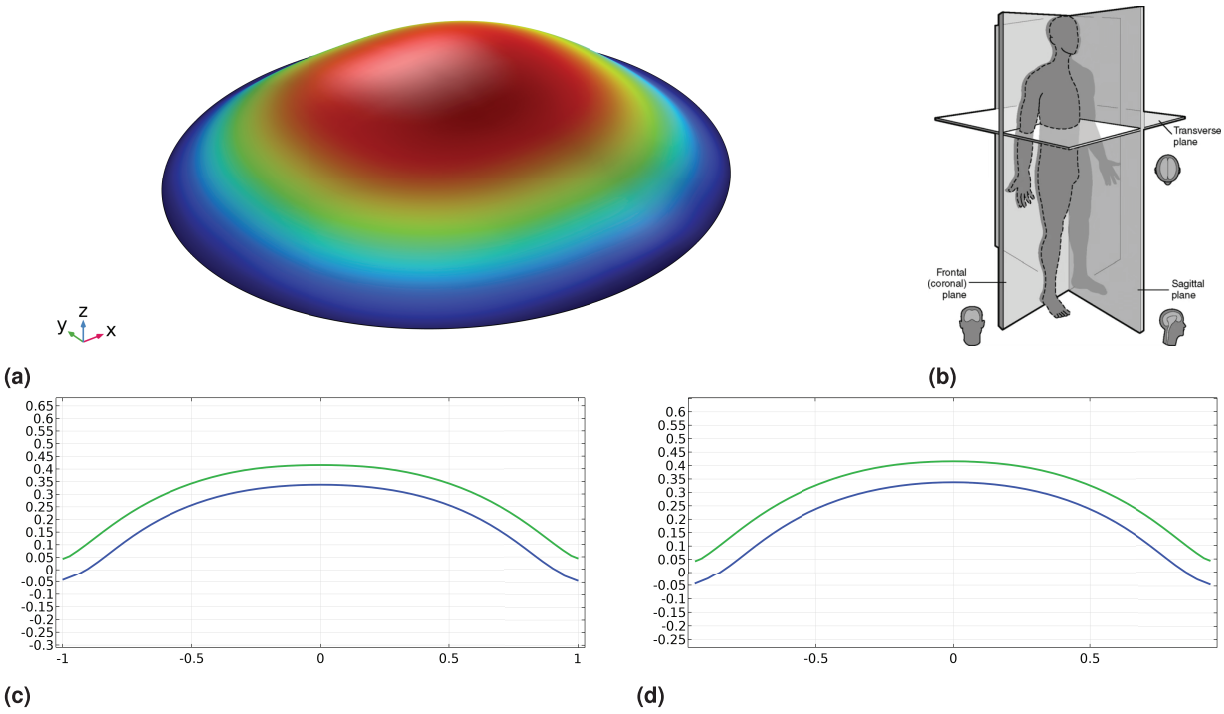

Figure 13. Equilibrium shape of a healthy cornea under the pressure of the aqueous humour: (a) perspective view, (b) definition of cutting planes, (c) transverse cut, (d) sagittal cut.

weight $\rho_A^* \boldsymbol{g}$. Herein, the mass density per unit area is set to be 0.504 kg/m^2 [35], where we assumed a characteristic thickness for the cornea of 480 μm.

At first, we consider the reference case of a normal, healthy cornea as a benchmark for having the shape of the cornea in this significant state. The corneal model was constructed based on an idealised, slightly elliptical geometry (eccentricity of about 0.3412 with the major axis horizontal) representing a healthy human cornea.

The mesh considered for the discretisation is made with 10,240 quadrilateral elements solved for 251,310 degrees of freedom. The interpolation functions employed for the discretisation of the two kinematical descriptors, namely, the displacement $\boldsymbol{u}$ and thickness field $\boldsymbol{d}$, are quadratic Lagrangian polynomials. This is because the energy requires shape functions that belong to at least the Hilbert space H^1 (for further details on relevant numerical methods, refer to, e.g., the works by Greco et al. [36], Cuomo and Greco [37], Greco and Cuomo [38], Battista et al. [39], and Dell'Erba et al. [40]).

4.1. The case of $\mathbb{C}_1 = 0$.

In the first scenario, we assume a case where the stiffness does not change along the transverse corneal direction. Specifically, we apply a uniform dimensionless pressure of 0.015 using the stiffness tensor evaluated with the engineering constants shown in Figure 11 with clamped boundary conditions ($\boldsymbol{u} = \boldsymbol{0}$ and $\boldsymbol{d} = \boldsymbol{N}$). The simulation results are shown in Figure 13. The figure features a perspective view of a healthy cornea, along with two sections aligned with the transverse and sagittal planes, which illustrate the reconstruction of thickness via the variable $\boldsymbol{d}$. Due to the symmetry of the problem, the two cut profiles are nearly identical.

Second, we conducted a parametric analysis to study the effect of the internal pressure surplus on the deformed shape of the corneal surface, considering varying pressure values. In Figure 14, the two surfaces delimiting the cornea along the horizontal cut for the pertained pressure are displayed. The cuts related to the sagittal direction are very similar; thus, for the sake of brevity, we omit them here.

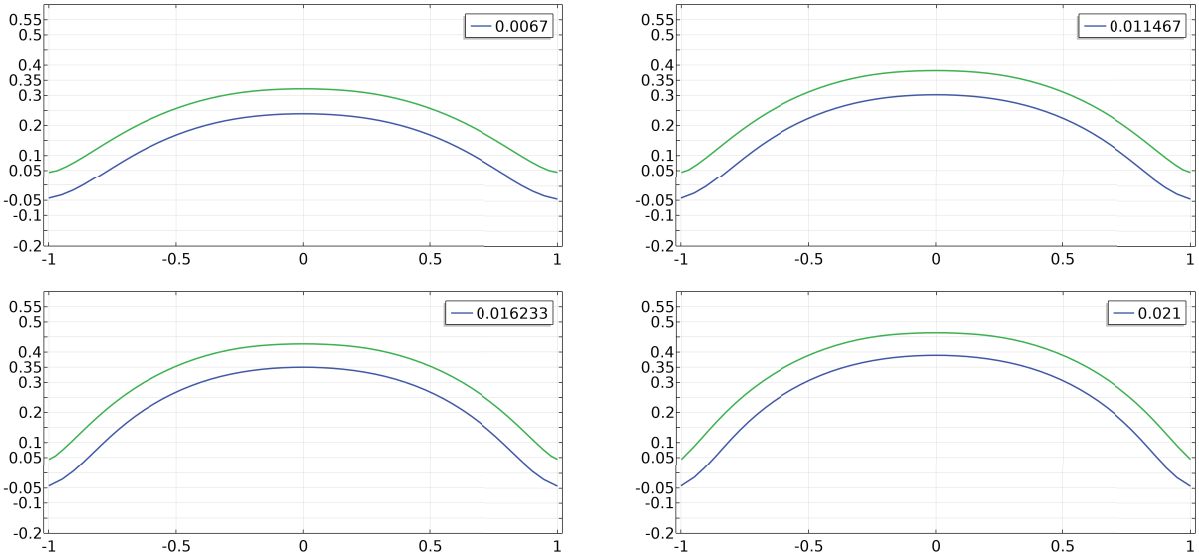

Figure 14. Transverse cuts for the reference cornea with different values of inner dimensionless pressure.

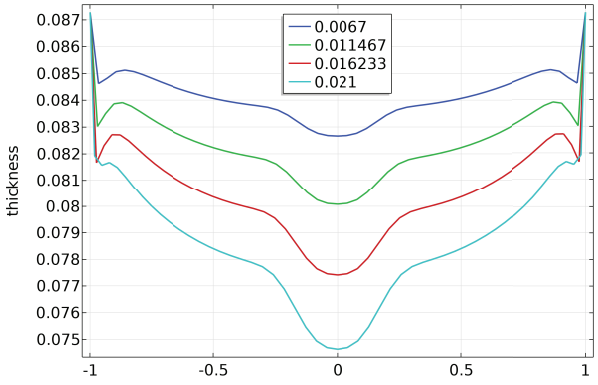

Figure 15. Thickness of the cornea for different pressures on the transverse plane.

To compare the results, we plot the diverse resulting thickness of the cornea under the pressures taken into account. From Figure 15, overall, the thickness appears to be uneven: a little smaller at the centre due to the larger stiffness localised there; a noticeable boundary layer is also detected due to the considered boundary conditions (in generalised continua it is possible to study the modalities and situations in which boundary layers arise, see, e.g., Laudato et al. [41], Barchiesi et al. [42], Eremeyev et al. [43]). Besides, the increase in the pressure acting on the inner part of the cornea causes the tissue to become thinner accordingly.

The presented analysis may be of interest in studying the effects of high eye pressure on corneal tissues.

4.2. *The case of* $\mathbb{C}_1 \neq 0$.

In the work by Pandolfi and Holzapfel [2], it is shown how one should expect that the mechanical properties are also varying in the transverse direction of corneas. Therefore, coherently with the approximations assumed in the present work, we allow for a (linear) variation of the stiffness tensor $\mathbb{C}$ with respect to X^3. In the case of healthy corneas, though, due to the symmetry of the problem, there is no noticeable difference in the equilibrium shape of the cornea. However, this could change when some more significant damage mechanisms due to the pathology of keratoconus do appear.

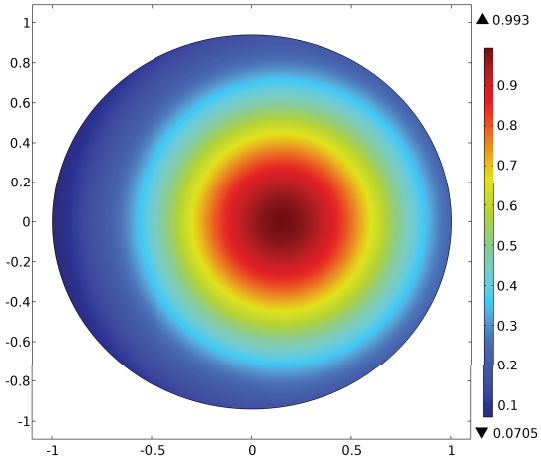

Figure 16. Case 1: Damage γ applied to the elastic moduli in the simulations centred inside the stiffer region.

It has also to be remarked that it is conceivable to study the mechanical properties of both healthy and keratoconus corneas by using measurements based on wave propagation inside them. With a reasonably accurate analysis, we believe that it will be possible to obtain this result by using the methods presented in the works by Turco and Barchiesi [44] and Ciallella [45], Eugster [46], and Yildizdag et al. [47], where it is proposed to characterise the mechanical behaviour of generalised continua by observing the modalities in which waves are propagating inside them.

5. Effects of non-uniform pathologically induced damage on cornea deformed shapes

It has been observed that in keratoconus corneas, the bulge always occurs in the lower part. It has been postulated that this may be caused by anatomical and structural differences between the superior and inferior parts of the cornea. The last one is biomechanically weaker than the superior cornea. In the works by Elsheikh et al. [48] and Meek et al. [49], it has been shown there is less collagen cross-linking and lower structural rigidity in the inferior portion, making it more prone to ectatic deformation, i.e., a structural change involving thinning and bulging of the tissue. Moreover, the collagen lamellae in the superior cornea are more tightly packed and organised compared to the inferior region, adding to the structural disparity [50]. For the seek of simplicity, in this section, we assume the presence of a fixed externally applied ocular pressure on one side of the cornea greater than atmospheric pressure, and we postulate some space variation, controlled via a few parameters, for the fields of the stiffnesses parameters, characterising the fourth-order tensor $\mathbb{C}$ and examine how varying aforementioned parameters one can get different equilibrium forms and thicknesses. We are aware of the fact that a more detailed model is necessary to better describe experimental evidence.

The here postulated mechanism explaining keratoconus-induced deformation of the cornea is simple: some corneal regeneration mechanisms fail to be activated, or some degeneration process starts, and it is maximum in a point and then has decreasing effects with the distance from such a point.

This possible explanation of the mechanical effects of keratoconus needs to be substantiated by detailed clinical and biological investigations: to our knowledge, no clear evidence is available to support it yet. The theoretical predictions formulated here may help in assessing it.

Notably, in the following numerical simulations, a field γ, measuring damage, has been introduced, and thus, the elastic moduli $(Y_1, Y_2, Y_3, \mu_{12}, \mu_{13}, \mu_{23})$ have been multiplied by $(1-\gamma)$ to take into account for the effect of such damage (see Figure 16). The shape of the damage has been chosen as a Gaussian function in order to quickly set the centre of the damage and its extension.

Figure 17 exhibits the equilibrium shape, with $\mathbb{C}_1 = 0$, and a physiological uniform pressure, together with the two main cuts, transverse and sagittal, with the damage of Figure 16. Here, the damage peak is placed horizontally in correspondence with the fibres that, in the same direction, give more stiffness to the cornea. Therefore, the effect of such damage is more recognisable in the transverse plane, with

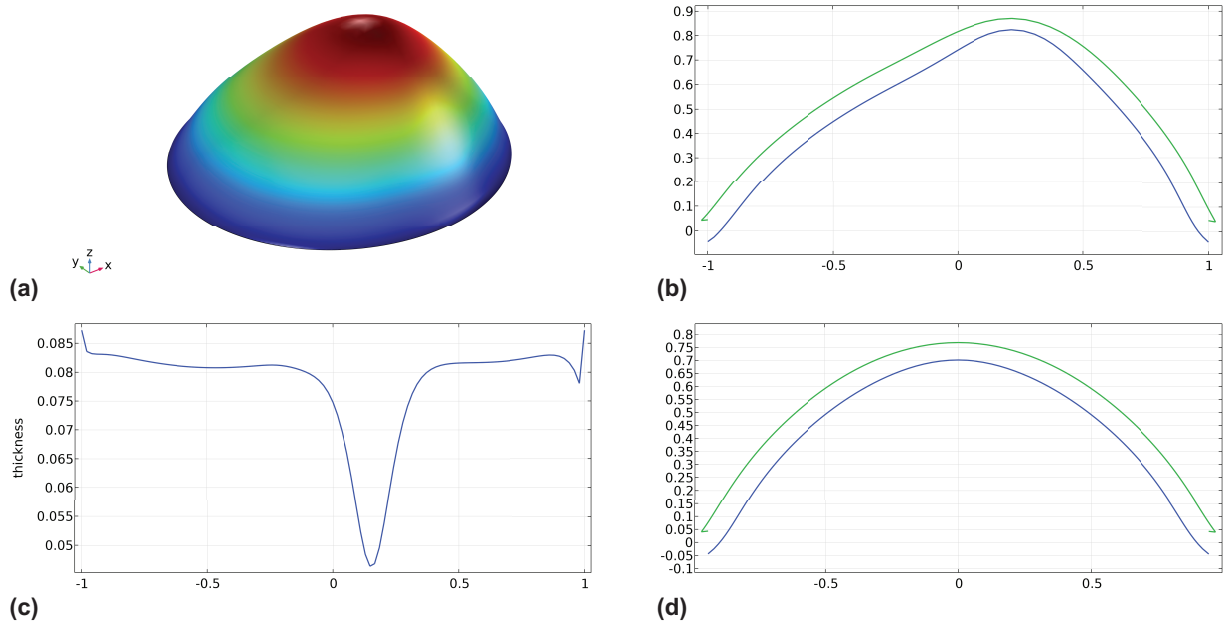

Figure 17. Case 1: Equilibrium shape of a cornea affected by keratoconus with a broad, non-uniform assumed damage: (a) perspective view, (b) transverse cut, (c) thickness in the transverse plane, (d) sagittal cut.

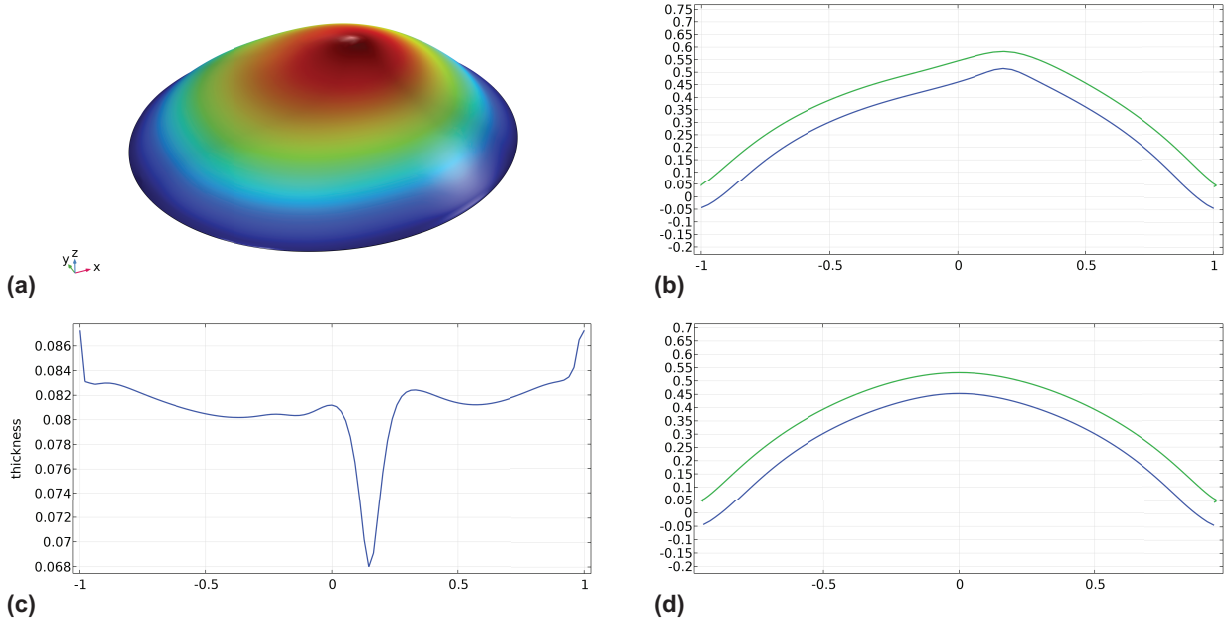

Figure 18. Case 2: Equilibrium shape of a cornea affected by keratoconus with a localised, non-uniform assumed damage: (a) perspective view, (b) transverse cut, (c) thickness in the transverse plane, (d) sagittal cut.

a thickness reduction at the maximum damage point in conjunction with a pronounced swelling in the same location (see Figure 17(c)).

In a second case, we halve the spatial extension of the damage while maintaining the same centre placement and amplitude to observe how the damage will localise its effects based on its location. These effects are clearly detected from the plots in Figure 18, where the perspective view of the middle surface of the cornea is displayed, together with the corneal sections in the transverse and sagittal planes, and the above-mentioned localisation of the thickness decrease.

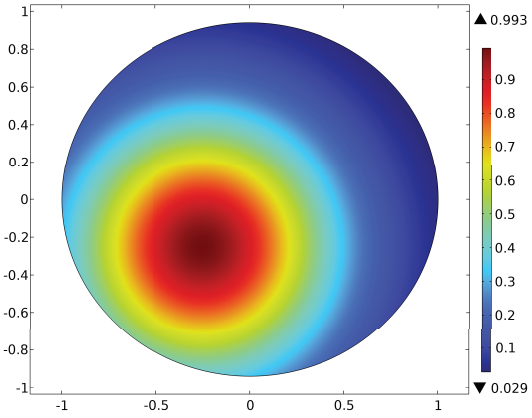

Figure 19. Case 3: Damage γ applied to the elastic moduli in the simulations centred in the less stiff region.

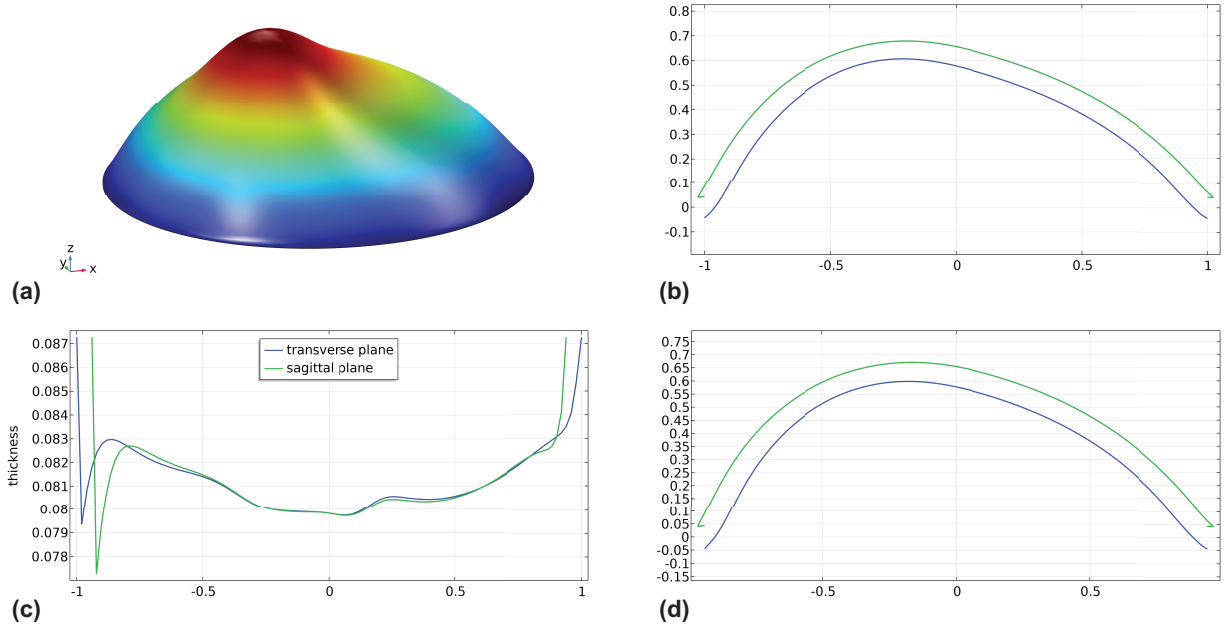

Figure 20. Case 3: Equilibrium shape of a cornea affected by keratoconus with non-uniform assumed damage in the soft region: (a) perspective view, (b) transverse cut, (c) thickness in the transverse and sagittal planes, (d) sagittal cut.

Afterwards, a third case is examined, changing the centre of the damage. In this scenario, we assume that the centre of the damage affects the less stiff region far from the fibre-reinforced two central bands (see Figure 19).

Figure 20 presents the outcomes of the new case, commencing from the overall middle surface of the cornea, which exhibits a bulge where the damage peak is situated. Figure 20(b)–(d) displays the transverse and sagittal sections of the cornea and the thickness in the corresponding planes, respectively. In these pictures, the thickness does not reduce excessively since the fibre-reinforced central bands still have their beneficial effect. Clearly, the thickness decreases the most in the damaged region, making the shape of the cornea less symmetrical.

Considering $\mathbb{C}_1 \neq 0$, a further case is examined to analyse the effect of stiffness variability across the cornea thickness. Here, the pattern of the engineering constants used to evaluate $\mathbb{C}_1$ is the same as for $\mathbb{C}_0$ but with a reduction factor scale of 1/8. Regarding the other settings, they are the same as in case 1. However, due to the more sensitive dependence on the damage, the amplitude of the damage is reduced a little to have a damage peak of 0.985. This will prevent the simulation from having numerical issues due

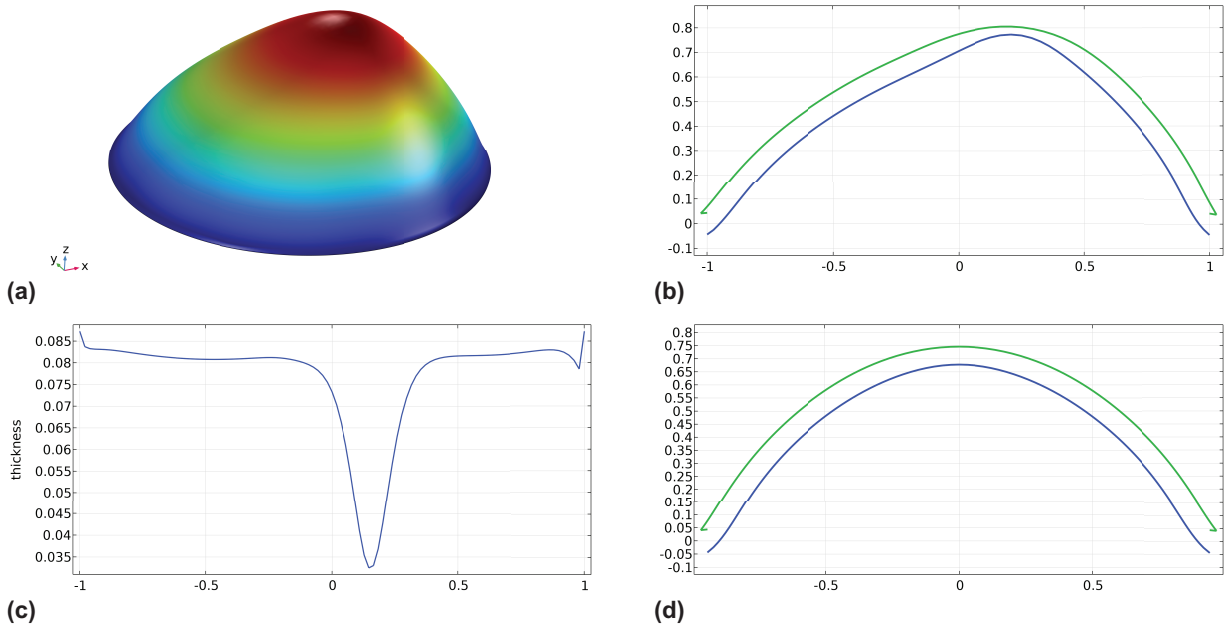

Figure 21. Equilibrium shape of a cornea affected by keratoconus with non-uniform assumed damage and mechanical properties varying in the transverse direction ($\mathbb{C}_1 \neq 0$): (a) perspective view, (b) transverse cut, (c) thickness in the transverse plane, (d) sagittal cut.

to the undesired approach to some singularities in the stiffness tensor. Overall, the behaviour is similar to case 1, as shown in Figures 21(a), (b), and (d) that provide the complete shape and the main cuts of the cornea. Nevertheless, the difference in thickness is evident (see Figure 21(c)), and we can clearly observe a more pronounced reduction here than in the previous case 1 due to the degeneration process.

In this section, we show how the presented model, eventually modified to improve its predictivity, may be used to test the validity of the assumed etiological mechanism for the onset of keratoconus: i.e., a degeneration of corneal tissue which is centred in a specific part of its tissue.

It is, however, our opinion that such a hypothesis is unlikely to be verified by further experimental and theoretical analyses because it is tough to explain why the degenerative process is always localised in a specific corneal part while assuming an influence on considered phenomena due to multiple factors, among them also related to external forces (such as eyelid stress), could allow for an easy prediction of many aspects of the observed phenomenology.

6. Effects on deformed shapes of eyelids mechanical action, weight, and uniform damage

Another postulated cause of the lower bulging of keratoconus corneas is related to eyelid mechanical effects. Blinking and eyelid pressure during normal eye movement may offer some shaping force to the superior cornea, as the upper eyelid covers more of the superior cornea, exerting an estimated pressure ranging between 10 and 80 mmHg [51,52], possibly stabilising it but exerting a vertical force on the cornea, whereas the lower cornea is more exposed and less supported, making it more susceptible to deformation.

Therefore, in this section, always assuming the presence of fixed externally applied eye pressure (equal to 0.012 normalised by 0.2 MPa), we postulate a decrease in corneal stiffness parameters, the application of a vertical force per unit area (set to 0.02166 normalised by 0.2 MPa) due to eyelid mechanical action on the superior cornea (see Figure 22), and the term modelling gravitational dead loads of both the cornea and aqueous humour in the external work functional. The dimensionless specific weight of aqueous humour is set to $6.4084 \times 10^{-4}\, X^2/L_0$ and is applied only in the inferior part of the cornea. It depends on the variable X^2 since the height of the liquid column can be roughly approximated as equal to $2\,X^2$,

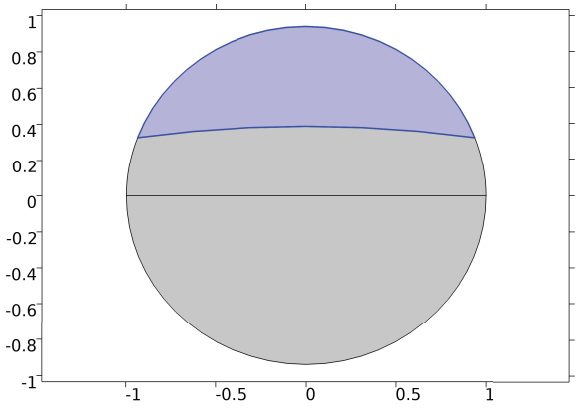

Figure 22. Application area of mechanical eyelid action.

thinking of the cornea as a sphere-like shell. Here, we assumed the mass density of the aqueous humour equal to $1005\,\mathrm{kg/m^3}$.

This analysis should be in agreement with the observation that keratoconus induces bulge deformations only in the lower part of the corneas.

Moreover, it may seem more logically economic to assume that the corneal regeneration failure or degeneration process is uniform and that the observed corneal bulging in keratoconus is driven by weight: however, as these actions may concentrate more fluids on the inferior cornea, the postulation that the inferior cornea may be more damaged in keratoconus is not entirely unfounded.[7]

Of course, our modelling postulate here is based on a drastic simplification: We study only elastic deformations of the considered 2D generalised continuum. We refrain, preliminarily, from investigating the complex damage pathological progression phenomena and the correspondingly induced plastic and permanent corneal deformation. We assume that the growth and regeneration phenomena (to be modelled in the future, by means of the methods presented, e.g., in the works by Grillo and Di Stefano [9, 10] also on the considerations given by Tepedino [11]) will shape permanently the cornea in a way which is "driven" by the elastic solutions which we have found in the present paper.

A first scenario is faced in this section simply considering uniform damage affecting the elastic modulus Y_3 set equal to 0.00169 (normalised by 0.2 MPa), considering the other elastic and shear moduli constant and equal to the minimum value of the healthy case. In this way, we assume that the degeneration process occurring in keratoconus weakens the two cross bands characteristic of the cornea structure, which loses greater stiffness as the orientation of the collagen fibres ceases to be aligned in the two main directions of orthotropy. In addition, we set $\mathbb{C}_1 = 0$ and fully clamped boundary conditions ($\boldsymbol{u} = \mathbf{0}$ and $\boldsymbol{d} = \boldsymbol{N}$). As it can be seen from Figure 23, the overall equilibrium shape is different from the previously considered cases. Here, we observe a thinning in the inferior part with a lack of symmetry and a certain level of bulging of the corneal structure, driven by the external load acting towards the vertical direction. Figure 23(b)–(d) shows the main sections along transverse and sagittal planes as well as the thickness in the same planes, respectively.

The same test is performed, solely changing the boundary conditions from fully clamped to simply supported, allowing the vector field $\boldsymbol{d}$ to rotate freely at the boundary. Figure 24 shows the new results. Compared to the previous case, these numerical calculations exhibit differences, which are clearly near the boundary, highlighting the notable importance of accurately modelling the boundary conditions.

Afterwards, the same simulation with $\mathbb{C}_1 \neq 0$ again with the clamped boundary conditions, as performed in the previous section, is conducted here to test the effect of stiffness variability across the thickness of the cornea. Overall, the qualitative behaviour, as depicted in Figure 25, exhibits a mildly different pattern, characterised by a slightly reduced thickness in comparison with the preceding example.

The presented simulations allow us to conclude that (1) inhomogeneous damage depending on (X^1, X^2) does not seem an effective and logically reasonable explanation of the onset of keratoconus (2) homogeneous (X^1, X^2) damage together with vertical loads effects seem a more economical thought explanation

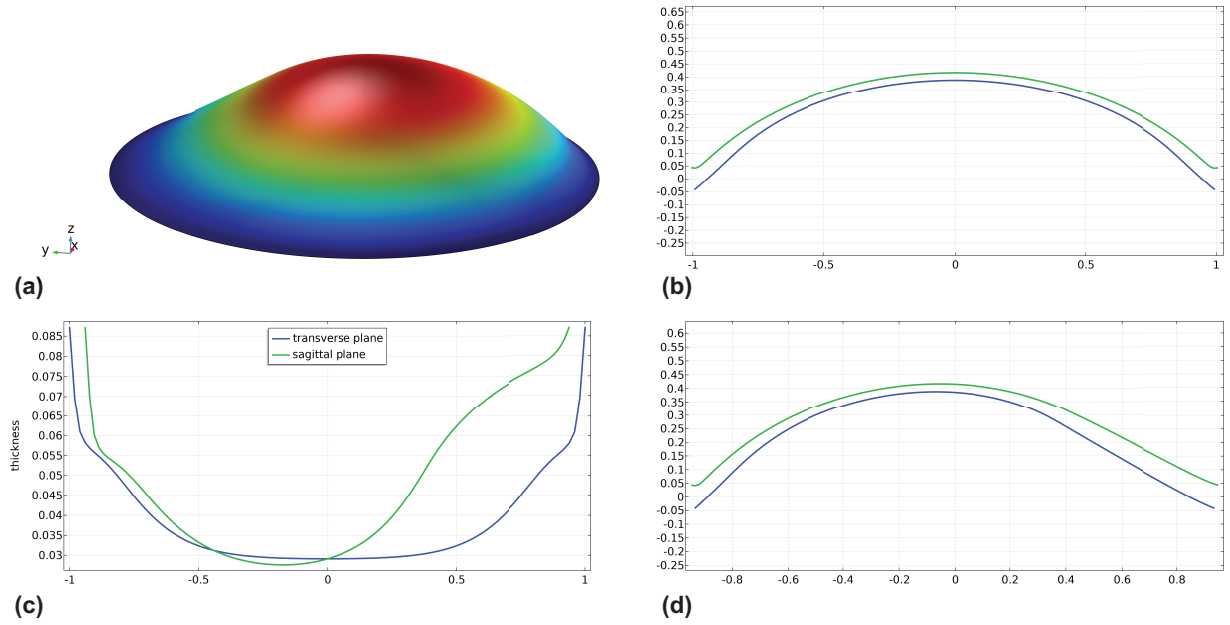

Figure 23. Equilibrium shape of a cornea affected by keratoconus with uniform damage, under the effect of weight, and $\mathbb{C}_{\mathrm{I}} = 0$, case of clamped BC: (a) perspective view, (b) transverse cut, (c) thickness in the transverse and sagittal planes, (d) sagittal cut.

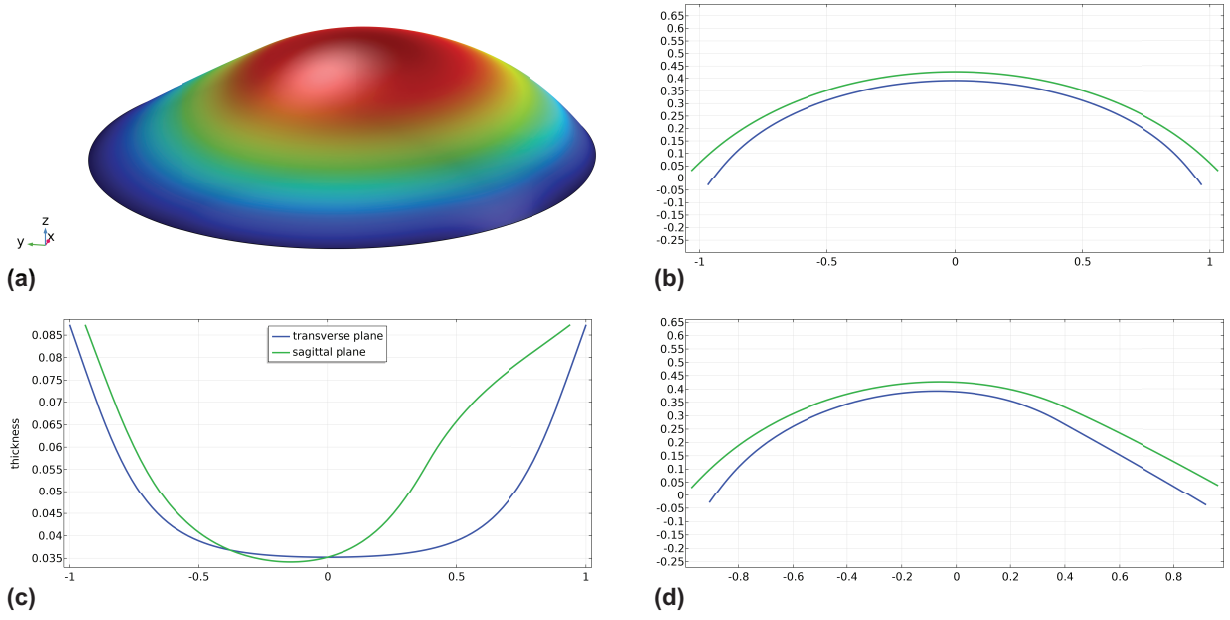

Figure 24. Equilibrium shape of a cornea affected by keratoconus with uniform damage, under the effect of weight, and $\mathbb{C}_{\mathrm{I}} = 0$, case of simply supported BC: (a) perspective view, (b) transverse cut, (c) thickness in the transverse and sagittal planes, (d) sagittal cut.

for the keratoconus corneal shape (3) albeit histological evidence shows that in keratoconus corneas the damage may depend on X^3 the postulate linear dependence on X^3 of the stiffness tensor does not affect too much keratoconus cornea shape: this means that more realistic X^3 dependences must be determined.

Moreover, the results presented in this section show that it is really necessary to improve our modelling procedure to include damage onset and growth so that the whole degenerative process, driven by the considered vertical loads, can be fully described.

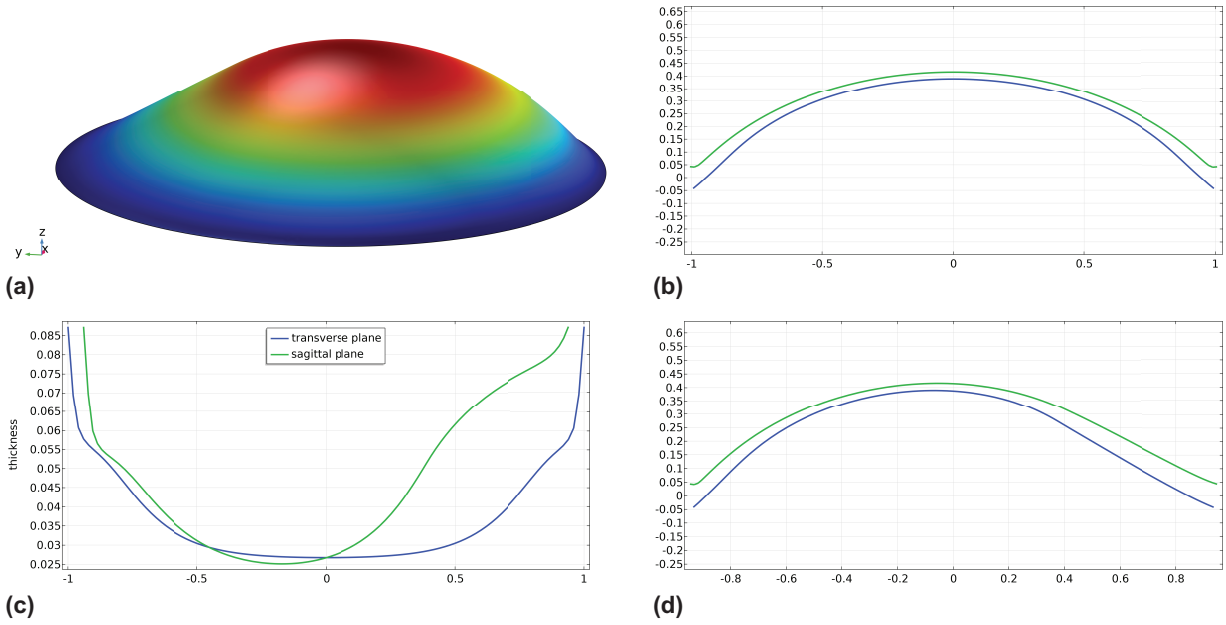

Figure 25. Equilibrium shape of a cornea affected by keratoconus with uniform damage, under the effect of weight, and with $\mathbb{C}_{\mathrm{I}} \neq 0$, case of clamped BC: (a) perspective view, (b) transverse cut, (c) thickness in the transverse and sagittal planes, (d) sagittal cut.

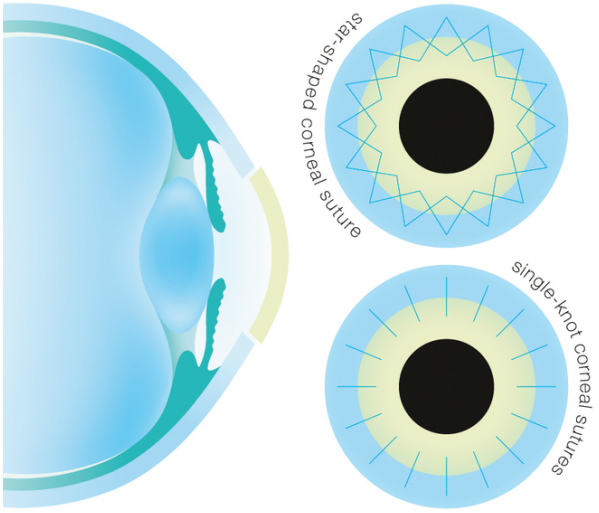

Figure 26. Geometry of penetrating keratoplasty.

7. Towards the mechanics of corneas after penetrating keratoplasty

Perusing [53], one can get an idea of the clinical importance of the considered problem. In the United States, the number of penetrating keratoplasty surgeries in the last decade has been about 30,000 operations per year.

As described in the work by Gurnani and Kaur [54], the penetrating keratoplasty (see Figure 26) consists of the replacement of the whole central corneal tissue with a donor's one. A suture will favour the formation of a cicatrix between the donor's and host's tissues.

7.1. The mechanical model for transplanted corneas using penetrating keratoplasty

The continuum model, which we introduce in this section, is characterised as follows:

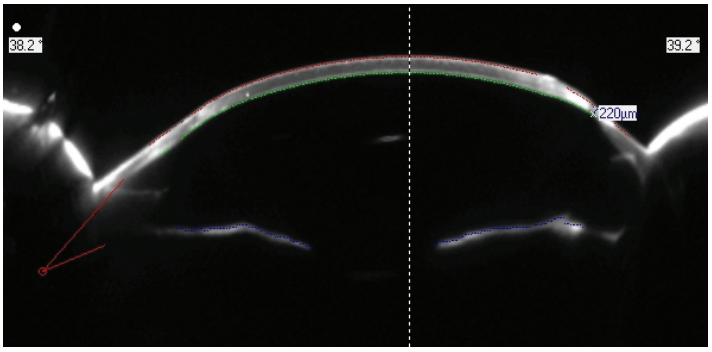

Figure 27. The transplanted cornea shape after a rather successful penetrating keratoplasty.

- The central corneal tissue is modelled as the "standard" material describing the mechanics of corneas.
- The peripheral region of the residual host corneal tissue is modelled as a "weaker" material, having the same material symmetry as the healthy corneas.
- The region of the suture, which becomes a cicatricial tissue, is modelled as a material with linearly variable moduli between the two previously mentioned ones (which, however, has the same material symmetries as the corneal tissue).
- The subjacent 3D continuum, which is used to obtain the reduced-order 2D generalised continuum after our micro-macro identification procedure, will be, therefore, assumed to be characterised by three different elasticity fourth-order tensors. In fact, we will assume that its constitutive equations include only geometric nonlinearities, being the elastic deformation energy a quadratic function of the finite deformation measures.

It has to be remarked that because of the known complex multi-scale microstructure of corneal tissue and also because of the presence of high gradients in material properties, in future developments, it could be beneficial to introduce second- or higher gradient 3D continuum models, as those studied numerically and mathematically in Laudato et al. [41], Eremeyev et al. [43], Abali et al. [55], Eremeyev and Altenbach [56], Abali [57], Abali et al. [58] and in Auffray et al. [18], Eremeyev et al. [59], Eremeyev [60], Eremeyev and Lazar [61], Dell'Isola et al. [62], Abdoul-Anziz and Seppecher [63] from the viewpoint of theoretical mechanics.

7.2. Commented results of numerical simulations

Experimental evidence shows that two possible outputs are occurring after penetrative keratoplasty. If the host corneal tissue is strong enough, we have the formation of a reasonably "regular" corneal shape, with the transplanted cornea having a nearly constant thickness (see Figure 27). Remark that the thinner part of the original keratoconus tissue has a thickness of 220 µm, and the residual astigmatism and hyperopia, albeit being more than 19 and 6 diopters, respectively, can be corrected with standard eyeglasses.

Instead, when parts of the host corneal tissue are so weak and thin that it cannot "maintain" a regular shape of the transplanted corneal tissue (see Figure 33), then the optical correction may become impossible even with scleral lenses.

It is, therefore, imperative to be able to predict the final shape of a transplanted cornea and it is clear that the study of the mechanical aspects of the related phenomena is essential.

Using our very simplified model, we show the predicted shapes of transplanted corneas in the case of very weak or sufficiently strong host corneal tissue.

7.2.1. The case of sufficiently strong host corneal tissue. To simulate the case of a transplanted cornea with a rather successful penetrating keratoplasty, we alter the dimensionless engineering constants, as described above, in the way which is represented by Figure 28, where the differences with the values used in the previous section are made precise.

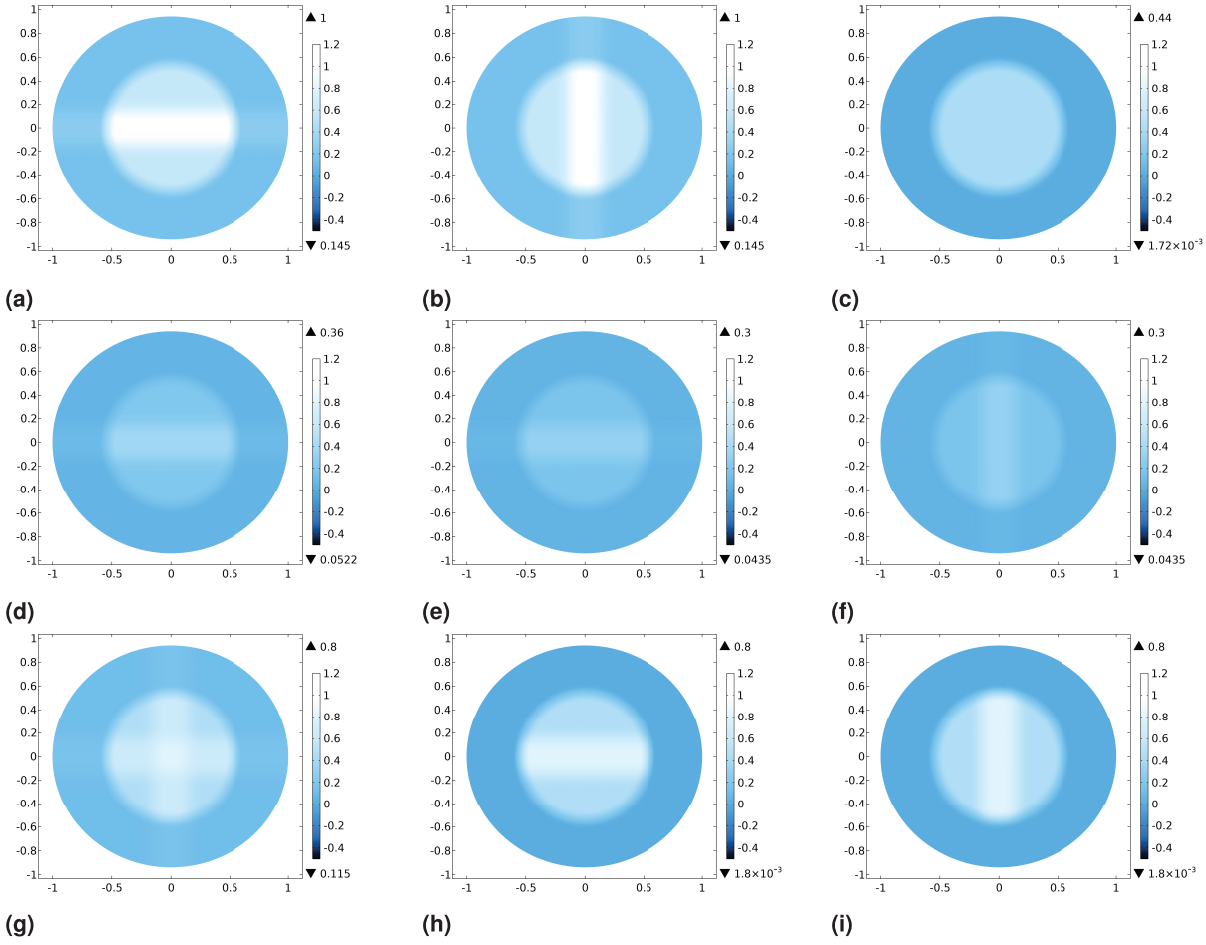

Figure 28. Modified dimensionless engineering constants: (a) elastic modulus Y_1, (b) elastic modulus Y_2, (c) elastic modulus Y_3, (d) Poisson ratio ν_{12}, (e) Poisson ratio ν_{13}, (f) Poisson ratio ν_{23}, (g) shear modulus μ_{12}, (h) shear modulus μ_{13}, (i) shear modulus μ_{23}.

Figure 29 shows the results of a numerical simulation with simply supported boundary conditions. We observe a localised slight decrease of the thickness of the cornea close to the cicatrices: however, this decrease is not "critical" as it is out of the center of the eye "optical" system and does not reach "rupture" values.[8]

To check the predictive ability of the proposed model, we compare the numerical simulations with the photos of a real transplanted cornea (see Figure 30). We have shown, with the blue and green lines, respectively, the internal and external surfaces of the predicted shape of the cornea, superimposed to the photo obtained with standard optical instruments: overall, the agreement seems acceptable. There are some discrepancies near the cicatrices, but overall, the trend is very good: the "true" cornea appears to be "thinner" there.

It has to be understood if this last fact is related to a thinner keratoconus cornea before transplant: in fact, these thin parts indeed belong to the original tissue suffering keratoconus and its thickness could have been reduced by the corresponding degeneration.

However, the initial findings suggest potential for improvement, and the results are promising, indicating that our investigations must be continued.

7.2.2. The case of a weak host corneal tissue. We also considered the case when the Young modulus Y_3 becomes very weak (in the simulation, we set a decreasing factor of 0.1) as well as an increase in the inner pressure of 50%. The corresponding results are shown in Figure 31. The boundary conditions for $\boldsymbol{d}$ are adjusted to match the varying thickness of the cornea, which is smaller on the top and increases towards the bottom. Specifically, we use a linear trend, with the reference value at the bottom and 1/4 at the top. We predict

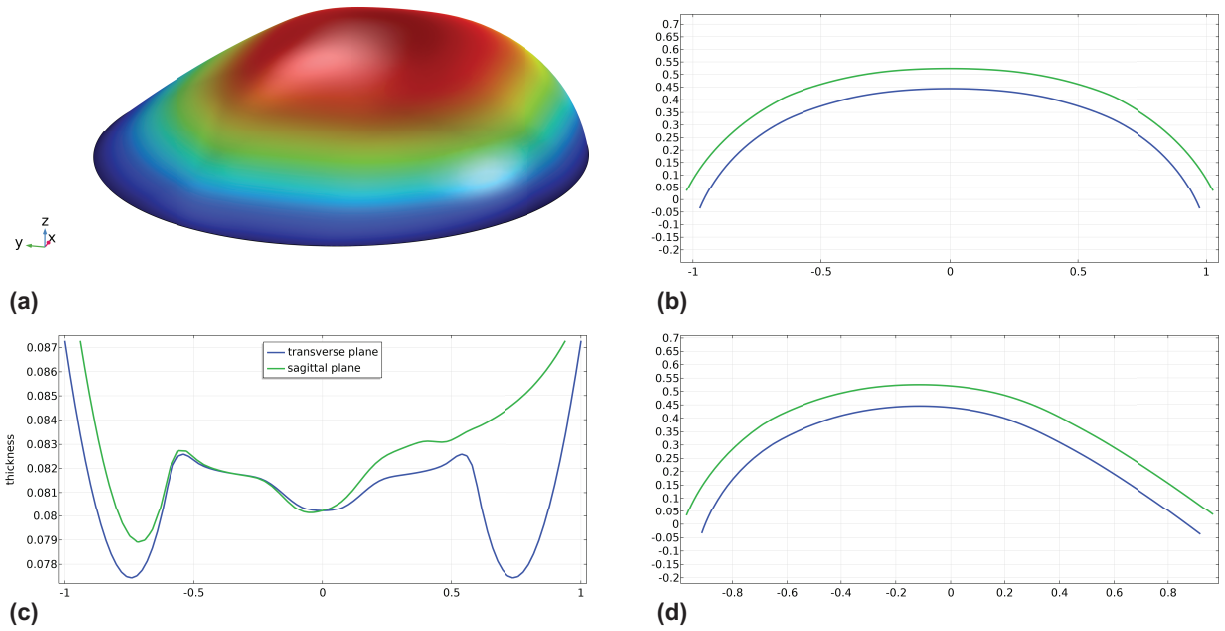

Figure 29. Case of sufficiently strong host corneal tissue: transplanted cornea shape: (a) perspective view, (b) transverse cut, (c) thickness in the transverse and sagittal planes, (d) sagittal cut.

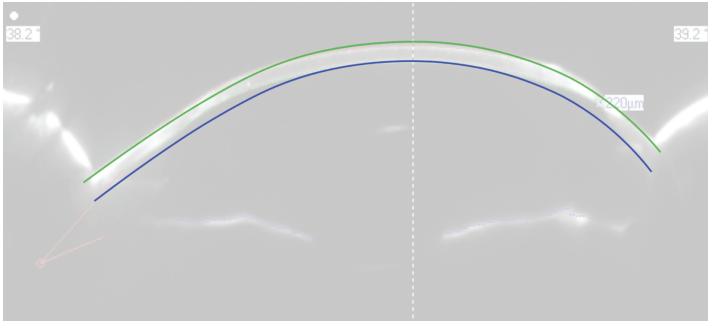

Figure 30. Case of sufficiently strong host corneal tissue: transplanted cornea shape (cut in the sagittal plane) comparison between numerical simulations and experimental evidence.

that the thickness of the corneal tissue significantly decreases: however, we observe that the localisation visible in the real scenario shown in Figure 32 is too challenging to be obtained with the model setting adopted here. In fact, the results seem to predict some qualitative aspects of the actual case, as shown, but the presented model needs substantial modification to better correspond with experimental evidence. We believe that the discrepancies between the predicted shapes and observed ones are related to the cylindrical symmetry hypothesis, which is clearly not entirely realistic when considering keratoconus corneas. A more predictive model will need to introduce measured extra-geometric properties of the considered system. In future investigations, we could also possibly assume that the initial thickness of the cornea before the surgery was already reduced. After the removal of the sick corneal tissue, the transplanted one is attached to an initially thinner layer in the corneal peripheral region. We also conjecture that the optimal fit will be achieved only by introducing second gradient continua, as clinical experience highlights the significant importance of observed boundary layers in the final equilibrium shapes of keratoconus and transplanted corneas. Indeed, the dimensions of these layers can be modelled by introducing appropriate characteristic lengths that can be clinically observed [42,64,65].

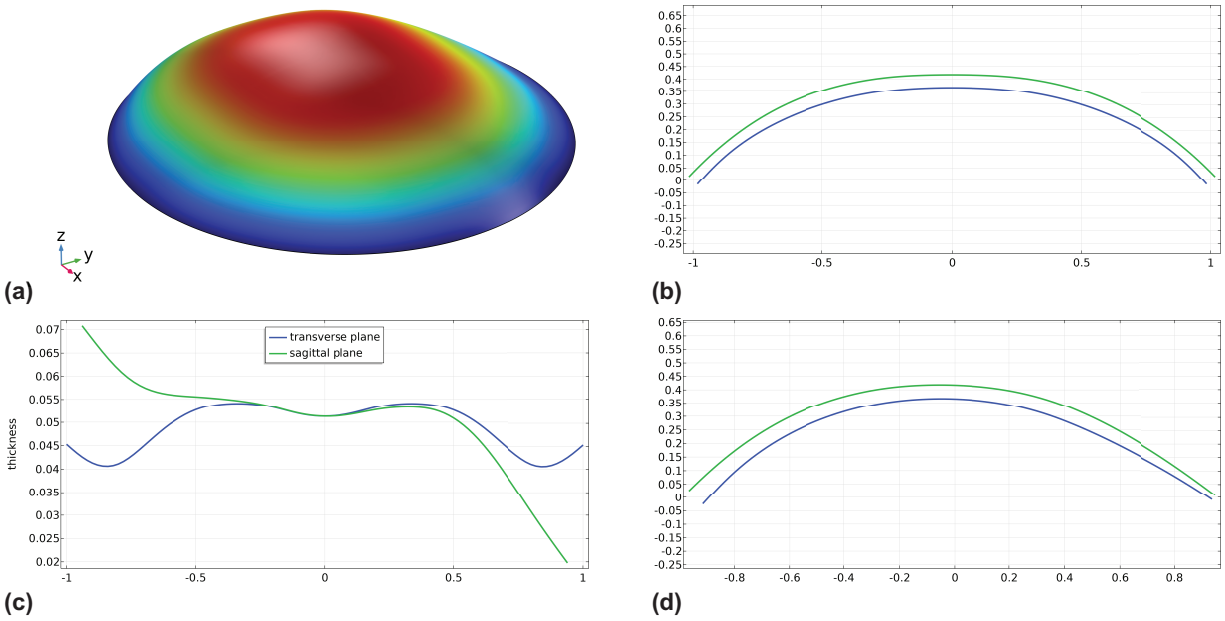

Figure 31. Case of transplanted cornea with weak Y_3: (a) perspective view, (b) transverse cut, (c) thickness in the transverse and sagittal planes, (d) sagittal cut.

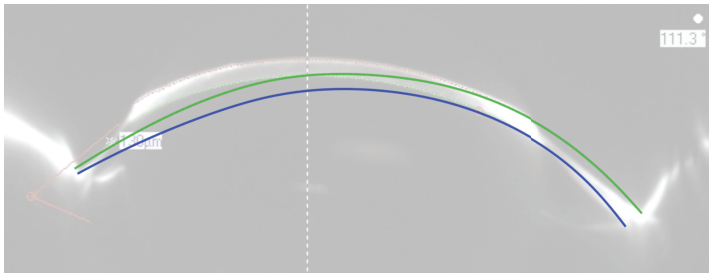

Figure 32. Case of a weak host corneal tissue: transplanted cornea shape (cut in the sagittal plane) comparison between numerical simulations and experimental evidence.

We also conjecture that the optimal fit will be achieved by incorporating higher gradient continua, as clinical experience highlights the significant importance of observed boundary layers in the final equilibrium shapes of keratoconus and transplanted corneas. Indeed, the dimensions of these layers can be modelled by introducing appropriate characteristic lengths that can be clinically observed.

It has to be underlined here explicitly that the issue of corneal thickness is of very relevant clinical importance. When the elastic moduli of the host corneal tissue are weak and result in a cornea that is too thin (say less than one-third of the physiological cornea), then one must expect very low optical qualities of the transplanted cornea. In fact, in humans, the refractive power of the cornea is approximately 43 diopters: if one considers that the cornea has a thickness of 520 μm one can conclude that 10 μm has an optical power of more than 0.82 diopters. In other words, minimal changes in shape may have an enormous optical effect. Consequently, the importance of the mechanical properties of transplanted corneas cannot be neglected.

8. Conclusion and research perspectives

In keratoconus, the bulge or cone-shaped protrusion of the cornea most commonly occurs inferiorly (in the lower part). The exact reason for this localisation is not fully understood: several theories and contributing factors may explain why this pattern tends to occur. We believe that a multifactorial explanation

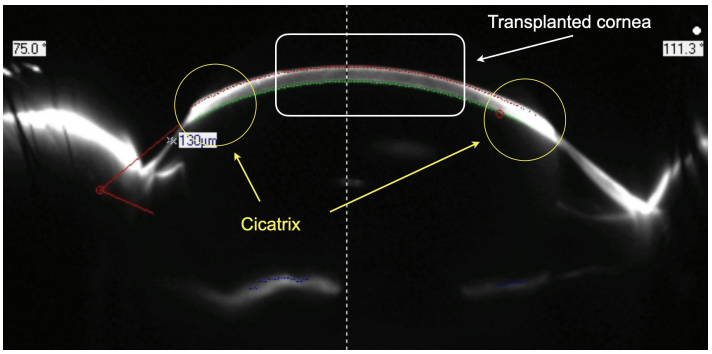

Figure 33. Transplanted cornea on weaker corneal tissue.

will be needed, and the present paper intends to contribute to such an explanation [66]. Indeed, there are anatomical and structural differences between the inferior and superior cornea [67], the first being mechanically weaker than the second one: there is experimental evidence that the collagen lamellae in the superior cornea are more tightly packed compared to the inferior cornea. Another factor may be the mechanical action of eyelids, which may be coupled with environmental and behavioural factors [68,69]. In fact, eye rubbing, especially in patients with allergies (very common in keratoconus), tends to be directed more toward the inferior cornea. This chronic mechanical stress can weaken that area further over time. Finally, it has been observed that genetic and biochemical factors may render the inferior cornea more prone to damage. Indeed, localised enzymatic imbalances (like increased MMPs and decreased protective enzymes) may have a more pronounced effect in areas that are already structurally weaker, and keratoconus is associated with oxidative stress and inflammatory markers, which may concentrate in mechanically stressed areas like the inferior cornea: all described factors are important potential factors of damage localised in the inferior cornea. In short, the inferior location of the cone in the keratoconus is likely due to a combination of anatomical weakness, mechanical exposure, and behavioural influences, all acting more on the lower part of the cornea.

In the present paper, a significant simplification has been accepted: no explicit plasticity or damage growth phenomena have been included, and no explicit models for the corneal tissue growth phenomena have been introduced. These simplifications have to be removed by using the techniques and results presented in the literature, e.g., by Grillo et al. [9,10]. We (simply and simplistically) assumed that the metabolically driven remodelling and growth phenomena occurring in human corneas follow the way which is indicated to them by the statical-equilibrium configurations calculated by using, albeit only geometrically non-linear, an elastic model.[9] In a more detailed model, one needs to describe (1) the process of growth of corneal tissues; (2) the process of metabolically induced mechanical damage of corneas affected by keratoconus; (3) the visco-elastic properties (using, e.g., the models presented in the works by Giorgio [70] and Cuomo et al. [71]) of corneas, at every stage of their degeneration; (4) all the relevant coupling among the previous phenomena.

When, instead, the complex system, which one wants to consider, is constituted by a transplanted central tissue, the tissue of the original cornea, which remains around the transplanted tissue and the cicatrix formed between them (see Figure 33) then the modelling challenges are even more formidable. The reader can see that, for the cornea considered in Figure 33, the residual original corneal tissue has a thickness of only 130 µm, while the transplanted tissue is much thicker and is closer to the physiological one: in fact, standard corneal thickness varies between 420 and 625 µm and the average thickness is 515 µm in the centre of the cornea. It has to be remarked that after transplant, the typical "drop-like" or "conical" shape of corneas affected by keratoconus is no longer present. We observe a weaker, nearly circular crown constituted by the original, weaker, and thinner tissue (i.e., the thinner part of the cornea represented in the photo 33). It is connected by means of a cicatrix (the internal white parts in the photo) to the transplanted part of the cornea (the internal dark part in the photo). In the present paper, we model the transplanted cornea (with penetrating keratoplasty) as follows: the subjacent 3D continuum used to obtain the reduced-order 2D generalised continuum modelling transplanted corneas has three different elasticity

fourth-order tensors. The one used to model the original tissue (i.e., the tissue affected by keratoconus) will be weaker, the tissue forming the cicatrix will be modelled with stiffer moduli, the central cornea (i.e., the tissue coming from the donor) will be considered to be constituted by a "standard" tissue.

In addition, we assume that the considered corneas have a non-stressed plane elliptic configuration and that the internal ocular pressure deforms the cornea, placing it in the actual configuration. This assumption simplifies our treatment: some undue and inappropriate simplifications may have been introduced because of it. In fact, the cornea, most likely, is not plane in its non-stressed configuration; therefore, to be more precise, when introducing its reference stress free-configuration in the 3D modelling, one has to consider a region, which is the union of segments of variable thickness, whose central points belong to an ellipsoid surface. As a consequence, the reduced order model should be what is called a "generalised shell" [13,14,72]. However, only after having proven in this paper that our approach gives well-grounded qualitative results, in future investigations, one is justified to relax these assumptions, also by using the methods presented in the works by Altenbach and Eremeyev [73], Altenbach et al. [74]. Of course, we are aware that in some modelling circumstances relevant to corneal mechanics, other external loads can be considered as line forces and point forces. As large deformations are unavoidable in the considered corneal mechanical equilibrium, then the analysis of the properties of third gradient continua, as performed by R. Fedele, seems necessary [64,65,75,76].

This paper considers two possible damage effects of keratoconus pathology on corneal shapes. Their plausibility needs to be checked with further clinical evidence: is the cone-like shape of keratoconus corneas caused by uniform damage of corneal tissue, and is its lower localisation related to gravitational forces and eyelid contact actions? or is it due to concentrated damage decreasing from a specific corneal localisation? We believe we have understood that the first possibility is more likely.

There are many research perspectives that are opened by the promising results presented in this paper. We limit ourselves to list those which seem to be the most immediate ones:

- A careful nondimensionalisation of a complete continuum higher gradient model seems necessary to investigate the possible performances of the continuum models by extensive parametric analysis and to identify the critical values of the biomechanical constitutive parameters introduced. The methods to be used are those presented in the works by De Angelo et al. [77] and Vazic et al. [78].
- A second or higher gradient 3D model seems necessary to describe the micro-behaviour of corneas, especially when the degenerative process induced by keratoconus causes locally high heterogeneities in constitutive parameters and regions where high gradients of displacement or plastic deformations [79–85] are concentrated. Indeed, the presence and onset of boundary layers within the deformed configurations of the studied continua, coupled with the remarkable heterogeneity of the material parameters inherent in keratoconus corneas, serve as well-established indicators [86–88] of the necessity for second gradient continuum models in the analysis of the specified mechanical system. Possibly even higher gradient models [64,75,76] may be necessary: a deeper theoretical investigation of these aspects may be required in determining the simplest generalised continuum model which is predictive enough to supply the demanded guidance to the understanding of considered phenomenology. The considered problem of keratoconus formation could also be viewed as a loss of stability under internal pressure, see the work by Eremeyev et al. [89].
- A numerical micro-macro identification is needed in order to base the continuum approach presented here on the discrete one presented in the papers [22–25] where the corneal fibres are modelled by means of a system of interconnected beams. The suggestive results presented there are qualitatively reproduced here; however, a quantitative micro-macro identification is demanded in order to connect more precisely the constitutive assumptions on the stiffness tensor $\mathbb{C}$ to the known properties of the corneal micro-structure. It has to be remarked that the statistical methods used, e.g., in the works by Soize [90] and La Valle et al. [91], will be necessary to attain such a result.
- An asymptotic expansion method seems, then, necessary to get an analytical micro-macro model identification and possibly lead to a rigorous homogenisation result. For the derivation of the highly deformable shells models, various techniques of the 3D-to-2D reduction are indeed possible Eremeyev et al. [15], Altenbach and Eremeyev [72] or Mühlich et al. [92], Mandadapu et al. [93]. In particular, the through-the-thickness integration procedure was successfully applied for derivation of thermo- and thermoviscoelastic shells, as well as shells with diffusion and phase transformations

[59,94–96]. For the methods needed to carefully determine the macro-constitutive parameters, we refer to the works by Abali and Barchiesi [97] and Vazic et al. [78] for homogenisation by using asymptotic analysis in mechanics and in thermomechanics Vazic et al. [98]. This analysis is also verified and applied in the works by Yang et al. [99] and Aydin et al. [100]. A comparison of different homogenisation techniques can be found in the work by Sarar et al. [101].

- A class of richer 2D reduced order models could be necessary to capture all relevant deformative and damage phenomena occurring in the pathogenic processes leading to keratoconus. We expect that together with the extra kinematical descriptor $\boldsymbol{d}$ some others may be required in order to usefully replace 3D with reduced order 2D models [96,102–107]. Such a model reduction, on the other hand, may be necessary if one has to confront a massive amount of simulations, either to explore the predictive possibilities of the model or to support and optimise the medical acts (as, e.g., transplants or surgical corneal shape corrections) aiming to the care of corneal pathologies.
- In the present paper, the 2D model is assumed to have as reference configuration a planar one. Albeit this assumption greatly simplifies the mathematical treatment, it may be considered simply as a first simplification that does not have a well-grounded physiological basis. Therefore, the generalised 2D plate theory used in the present paper needs to be refined by introducing a 2D generalised shell theory. With second gradient models, it is possible to compute [108] the shapes of generalised shells, overcoming some serious numerical challenges [79,109]. Therefore, we expect that reduced order models may also be used (see De Angelo et al. [77]) to describe our phenomenology.
- In the present work, the analysis is based on essential boundary conditions only. In other words, we assume that the cornea is "clamped" or that corneal tissue can rotate with respect to the rest of the *bulbus oculi* (i.e., the part of the sclera where the cornea is attached). We are aware of the fact that it is necessary to have more detailed modelling of the mechanical interactions between the cornea and the other structural elements of the ocular globe: this will be made possible by eventually introducing suitable and more complex natural or mixed boundary conditions.
- We conjecture that it will be possible to estimate the layered structure of the corneal tissue by studying and measuring the properties of waves propagating inside it (e.g., by using the methods presented in Eugster [46], Yildizdag et al. [47]). In this context, it seems reasonable that the corneal micro-structure may "trap" some of the kinetic energy of the "testing wave." Therefore, the methods presented in Abali et al. [58], Placidi et al. [110], Bersani et al. [111] may be helpful.
- Treatments for corneal issues depend on the type and severity of the condition. Among some common treatments, we can recall: medications with eye drops made by lubricating, steroid, and antibiotic drops commonly used to treat corneal infections (keratitis) or inflammations; laser treatment, namely, phototherapeutic keratectomy (PTK); corneal transplantation; stem cell therapy, for some severe injuries or degenerative diseases, stem cell transplants from the limbal region of the eye (the border between the cornea and sclera) can help regenerate damaged corneal tissue. Some ideas about how to model these treatments can be found in the work by Osorio-Blanco et al. [112], where enriched particles are studied, or in the work by Zhang et al. [113], where hydrogel is employed.

Declaration of conflicting interests

The author(s) declared no potential conflicts of interest with respect to the research, authorship, and/or publication of this article.

Funding

The author(s) received no financial support for the research, authorship, and/or publication of this article.

ORCID iD

Ivan Giorgio https://orcid.org/0000-0002-0044-9188

Notes

1. The socioeconomic impact of keratoconus should not be underestimated. In the work by Wagner et al. [114], it has been estimated that patients affected by keratoconus are expected to spend more than 25,000 $ in their post-diagnosis lifetime

if no transplant is necessary. In fact, the cost-benefit analysis performed by the Lewin Group for Eye Bank Association of America in 2013 estimated the cost of about 17,000 $ for each corneal transplant.

2. It seems that, in order to be able to "measure" the shape of keratoconus or transplanted corneas, some non-standard techniques need to be developed. This is a problem related to the other issue concerning the experimental "identification" and determination [115–119] of the mathematical models and the mechanical parameters most suitable for predicting the behaviour of mechanical systems. It has to be remarked that it seems necessary to develop the available techniques to face the problem of (1) identifying the mechanical properties of corneal tissues (as done, e.g., in Valmalle et al. [120, 121], Maier et al. [122], Fedele et al. [123]), and (2) being able to reconstruct the highly irregular shapes of keratoconus and transplanted corneas. In this context, it seems that the works by Hild and Roux give suitable conceptual and technical tools [115,118,124–126].
3. The presence of high gradients of deformation, stress, and material properties proven experimentally to be present in keratoconus and transplanted corneas will demand the introduction of high- gradient continua of the kind studied by Paul Germain [127] and developed in the literature [55,64,65,108,128–131]. It is to be noticed that the specific geometry of corneas and their mechanical interconnection with the sclera may indicate that third-gradient continua may be needed for successful modelling [75,76].
4. In this context the results presented in Olive and Auffray [132] are beneficial to characterise the constitutive equations of the material constituting corneas.
5. We acknowledge explicitly here the enlightening discussions with Proff. Vasta and Gizzi, who allowed us to formulate the just mentioned assumption. We believe that it has to be carefully investigated the relationship between their model, based on corneal truss "micro-architecture" and the continuum model that we present here. In this context, the methods and the results presented in the works by Alibert et al. [128] and Lubarda and Chen [21], Yildizdag et al. [47, 133], Spagnuolo et al. [134], Erden Yildizdag et al. [135] can be extremely useful.
6. For higher gradient generalised continua non-standard natural boundary conditions arise and must be determined via a process of integration by parts, as shown in the work by Germain [127] and, for third gradient continua, in the works by Fedele [75, 76].
7. Indeed, keratoconus is associated with an imbalance in matrix metalloproteinases (MMPs) and their inhibitors, resulting in localised stromal degradation. These biochemical changes may preferentially affect structurally weaker regions like the inferior cornea (Elsheikh et al. [48]).
8. It has to be remarked that the damage and rupture phenomena in transplanted and keratoconus corneas have not been completely understood, both from the biological and the mechanical viewpoints. We feel a particular need to develop mechanical models for the damage and plasticity occurring in corneal tissues by taking into account their "fibrous" microstructure (for relevant models already available in the literature, see, e.g., Spagnuolo et al. [119], Valmalle et al. [121], Maier et al. [122], Valoroso and Fedele [136], Ponomarev [137]).
9. The first author, affected by keratoconus and whose corneas were transplanted with a penetrative keratoplasty (see the previous Figures 6 and 7, which refer to his corneas), believe to see slight differences in his visual acuity if he changes the angle between his corneal sagittal direction and the weight direction. This may be related to the fact that, in weak corneas, the elastic deformations induced by the vertical mechanical actions may change the corneal optical properties. Of course, such an observation may have many different explanations and deserves to be substantiated by careful theoretical analysis and precise measurements. While T. Henze will find a practical way to perform such measurements, we suspend our judgment.

References

[1] Nottingham, J. *Practical observations on conical cornea, and on the short sight, and other defects of vision connected with it*. London: J. Churchill, 1854.

[2] Pandolfi, A, and Holzapfel, GA. Three-dimensional modeling and computational analysis of the human cornea considering distributed collagen fibril orientations. *J Biomech Eng* 2008; 130(6): 061006.

[3] Pandolfi, A, and Manganiello, F. A model for the human cornea: constitutive formulation and numerical analysis. *Biomech Model Mechanobiol* 2006; 5(4): 237–246.

[4] Pandolfi, A, and Vasta, M. Fiber distributed hyperelastic modeling of biological tissues. *Mech Mater* 2012; 44: 151–162.

[5] dell'Isola, F, Vasta, M, Gizzi, A, et al. 2D generalized continuum modeling cornea changes of shapes induced by pathogenetical process related mechanical damage. In: *Mathematical modelling in biology and medicine*, Arpino, Italy, 8–12 May, 2023.

[6] Epstein, A. Keratoconus and related disorders. *North Shore Contact Lens* 2000; 87: 87.

[7] Romero-Jiménez, M, Santodomingo-Rubido, J, and Wolffsohn, JS. Keratoconus: a review. *Cont Lens Anterior Eye* 2010; 33(4): 157–166.

[8] Hashemi, H, Heydarian, S, Hooshmand, E, et al. The prevalence and risk factors for keratoconus: a systematic review and meta-analysis. *Cornea* 2020; 39(2): 263–270.

[9] Grillo, A, and Di Stefano, S. Comparison between different viewpoints on bulk growth mechanics. *Math Mech Complex Syst* 2023; 11(2): 287–311.

[10] Grillo, A, and Di Stefano, S. An a posteriori approach to the mechanics of volumetric growth. *Math Mech Complex Syst* 2023; 11(1): 57–86.

[11] Tepedino, M. The mechanical role of the periodontal ligament for developing mathematical models in orthodontics. *Math Mech Complex Syst* 2023; 11(4): 525–539.

[12] Cogan, DG. Clinical physiology of the cornea. *Bull Ophthal Soc Egypt* 1953; 46: 484–498.

[13] Altenbach, J, Altenbach, H, and Eremeyev, VA. On generalized Cosserat-type theories of plates and shells: a short review and bibliography. *Arch Appl Mech* 2010; 80(1): 73–92.

[14] Altenbach, H, Eremeyev, V, et al. Actual developments in the nonlinear shell theory—state of the art and new applications of the six-parameter shell theory. *Shell Struct Theory Appl* 2014; 3: 3–12.

[15] Eremeyev, V, Pietraszkiewicz, W, et al. Refined theories of plates and shells. *Z Angew Math Mech* 2014; 94(1–2): 5.

[16] Eremeyev, VA, Lebedev, LP, and Cloud, MJ. The Rayleigh and Courant variational principles in the six-parameter shell theory. *Math Mech Solids* 2015; 20(7): 806–822.

[17] Pietraszkiewicz, W, Eremeyev, V, and Konopińska, V. Extended non-linear relations of elastic shells undergoing phase transitions. *Z Angew Math Mech* 2007; 87(2): 150–159.

[18] Auffray, N, dell'Isola, F, Eremeyev, VA, et al. Analytical continuum mechanics à la Hamilton–Piola least action principle for second gradient continua and capillary fluids. *Math Mech Solids* 2015; 20(4): 375–417.

[19] dell'Isola, F, Seppecher, P, and Madeo, A. How contact interactions may depend on the shape of Cauchy cuts in Nth gradient continua: approach "à la D'Alembert". *Z Angew Math Phys* 2012; 63: 1119–1141.

[20] Dell'Isola, F, Madeo, A, and Seppecher, P. Cauchy tetrahedron argument applied to higher contact interactions. *Arch Ration Mech An* 2016; 219: 1305–1341.

[21] Lubarda, V, and Chen, M. On the elastic moduli and compliances of transversely isotropic and orthotropic materials. *J Mech Mater Struct* 2008; 3(1): 153–171.

[22] De Bellis, ML, Vasta, M, Gizzi, A, et al. A numerical model of the human cornea accounting for the fiber-distributed collagen microstructure. *Math Mech Solids*. Epub ahead of print 8 November 2023. DOI: 10.1177/10812865231202024.

[23] De Bellis, ML, Vasta, M, Gizzi, A, et al. Modeling the deterioration of the stiffness and of the collagen fibril distribution in a discrete model of the cornea microstructure. *Int J Non Linear Mech* 2024; 163: 104736.

[24] Pandolfi, A, Gizzi, A, and Vasta, M. A microstructural model of cross-link interaction between collagen fibrils in the human cornea. *Philos Trans R Soc A* 2019; 377(2144): 20180079.

[25] Pandolfi, A, De Bellis, ML, Gizzi, A, et al. Modeling the degeneration of the collagen architecture in a microstructural model of the human cornea. *Math Mech Solids* 2023; 28(1): 196–207.

[26] Pye, DC. A clinical method for estimating the modulus of elasticity of the human cornea in vivo. *PLoS ONE* 2020; 15(1): e0224824.

[27] Shih, PJ, Huang, CJ, Huang, TH, et al. Estimation of the corneal Young's modulus in vivo based on a fluid-filled spherical-shell model with Scheimpflug imaging. *Journal of ophthalmology* 2017; 2017(1): 5410143.

[28] dell'Isola, F, Maier, G, Perego, U, et al. (eds) *The complete works of Gabrio Piola: Volume I. commented English translation. advanced structured materials*. Cham: Springer, 2014.

[29] Dell'Isola, F, and Kosinski, W. Deduction of thermodynamic balance laws for bidimensional nonmaterial directed continua modelling interphase layers. *Arch Mech* 1993; 45(3): 333–359.

[30] Boutin, C, and Viverge, K. Generalized plate model for highly contrasted laminates. *Eur J Mech A/Solids* 2016; 55: 149–166.

[31] Jakabčin, L, and Seppecher, P. On periodic homogenization of highly contrasted elastic structures. *J Mech Phys Solids* 2020; 144: 104104.

[32] Viverge, K, Boutin, C, and Sallet, F. Model of highly contrasted plates versus experiments on laminated glass. *Int J Solids Struct* 2016; 102: 238–258.

[33] Köry, J, Stewart, PS, Hill, NA, et al. A discrete-to-continuum model for the human cornea with application to keratoconus. *R Soc Open Sci* 2024; 11(7): 240265.

[34] Murgatroyd, H, and Bembridge, J. Intraocular pressure. *Conti Edu Anaesth Critical Care Pain* 2008; 8(3): 100–103.

[35] Ramier, A, Eltony, AM, Chen, Y, et al. In vivo measurement of shear modulus of the human cornea using optical coherence elastography. *Sci Report* 2020; 10(1): 17366.

[36] Greco, L, Cuomo, M, and Contrafatto, L. Two new triangular G1-conforming finite elements with cubic edge rotation for the analysis of Kirchhoff plates. *Comput Method Appl M* 2019; 356: 354–386.

[37] Cuomo, M, and Greco, L. An implicit strong G1-conforming formulation for the analysis of the Kirchhoff plate model. *Continuum Mech Therm* 2020; 32(3): 621–645.

[38] Greco, L, and Cuomo, M. An implicit G1-conforming bi-cubic interpolation for the analysis of smooth and folded Kirchhoff–Love shell assemblies. *Comput Method Appl M* 2021; 373: 113476.

[39] Battista, A, Rosa, L, Dell'Erba, R, et al. Numerical investigation of a particle system compared with first and second gradient continua: deformation and fracture phenomena. *Math Mech Solids* 2017; 22(11): 2120–2134.

[40] Dell'Erba, R, D'avanzo, P, and Rapisarda, AC. A comparison between the finite element method and a kinematic model derived from robot swarms for first and second gradient continua. *Continuum Mech Therm* 2023; 35(4): 1769–1786.
[41] Laudato, M, Manzari, L, Göransson, P, et al. Experimental analysis on metamaterials boundary layers by means of a pantographic structure under large deformations. *Mech Res Commun* 2022; 125: 103990.
[42] Barchiesi, E, Ciallella, A, and Giorgio, I. On boundary layers observed in some 1D second-gradient theories. In: Barchiesi, E, Ciallella, A, and Giorgio, I (eds) *Theoretical analyses, computations, and experiments of multiscale materials: a tribute to francesco dell'isola*. Cham: Springer, 2022, pp. 359–376.
[43] Eremeyev, VA, Lurie, SA, Solyaev, YO, et al. On the well posedness of static boundary value problem within the linear dilatational strain gradient elasticity. *Z Angew Math Phys* 2020; 71: 1–16.
[44] Turco, E, and Barchiesi, E. Kinematically triggered nonlinear vibrations of Hencky-type pantographic sheets. *Math Mech Complex Syst* 2022; 9(3): 311–335.
[45] Ciallella, A. Research perspective on multiphysics and multiscale materials: a paradigmatic case. *Continuum Mech Therm* 2020; 32: 527–539.
[46] Eugster, SR. Numerical analysis of nonlinear wave propagation in a pantographic sheet. *Math Mech Complex Syst* 2022; 9(3): 293–310.
[47] Yildizdag, ME, Sarar, BC, Salvatori, A, et al. Analysis of transmission and reflection characteristics of linear plane waves in pantographic lattices. *Z Angew Math Phys* 2023; 74(5): 178.
[48] Elsheikh, A, Wang, D, Brown, M, et al. Assessment of corneal biomechanical properties and their variation with age. *Current eye research* 2007; 32(1): 11–19.
[49] Meek, KM, Tuft, SJ, Huang, Y, et al. Changes in collagen orientation and distribution in keratoconus corneas. *Invest Ophthalmol Vis Sci* 2005; 46(6): 1948–1956.
[50] Romero-Jiménez, M, Santodomingo-Rubido, J, and Wolffsohn, JS. Keratoconus: a review. *Cont Lens Anterior Eye* 2010; 33(4): 157–166.
[51] Shaw, AJ, Collins, MJ, Davis, BA, et al. Eyelid pressure and contact with the ocular surface. *Invest Ophthalmol Vis Sci* 2010; 51(4): 1911–1917.
[52] Doane, MG. Interactions of eyelids and tears in corneal wetting and the dynamics of the normal human eyeblink. *American journal of ophthalmology* 1980; 89(4): 507–516.
[53] Mathews, P, Benbow, A, Corcoran, K, et al. 2022 eye banking statistical report—executive summary. *Eye Bank Corneal Transplant* 2023; 2(3): e1–e12.
[54] Gurnani, B, and Kaur, K. *Penetrating keratoplasty*. Treasure Island, FL: StatPearls Publishing, 2023.
[55] Abali, BE, Müller, WH, and Eremeyev, VA. Strain gradient elasticity with geometric nonlinearities and its computational evaluation. *Mech Adv Mater Mod Process* 2015; 1: 1–11.
[56] Eremeyev, VA, and Altenbach, H. On the direct approach in the theory of second gradient plates. In: Altenbach, H, and Mikhasev, GI (eds) *Shell and membrane theories in mechanics and biology: from macro-to nanoscale structures*. Cham: Springer, 2014, pp. 147–154.
[57] Abali, BE. Energy based methods applied in mechanics by using the extended Noether's formalism. *Z Angew Math Mech* 2023; 103: e202300020.
[58] Abali, BE, Vazic, B, and Newell, P. Influence of microstructure on size effect for metamaterials applied in composite structures. *Mech Res Commun* 2022; 122: 103877.
[59] Eremeyev, VA, Cazzani, A, and Dell'Isola, F. On nonlinear dilatational strain gradient elasticity. *Continuum Mech Therm* 2021; 33: 1429–1463.
[60] Eremeyev, VA. Strong ellipticity conditions and infinitesimal stability within nonlinear strain gradient elasticity. *Mech Res Commun* 2021; 117: 103782.
[61] Eremeyev, VA, and Lazar, M. Strong ellipticity within the Toupin–Mindlin first strain gradient elasticity theory. *Mech Res Commun* 2022; 124: 103944.
[62] Dell'Isola, F, Sciarra, G, and Vidoli, S. Generalized Hooke's law for isotropic second gradient materials. *Proc R Soc A Math Phys Eng Sci* 2009; 465(2107): 2177–2196.
[63] Abdoul-Anziz, H, and Seppecher, P. Strain gradient and generalized continua obtained by homogenizing frame lattices. *Math Mech Complex Syst* 2018; 6(3): 213–250.
[64] Fedele, R. Piola's approach to the equilibrium problem for bodies with second gradient energies. Part I: first gradient theory and differential geometry. *Continuum Mech Therm* 2022; 34(2): 445–474.
[65] Fedele, R. Approach à la Piola for the equilibrium problem of bodies with second gradient energies. Part II: variational derivation of second gradient equations and their transport. *Continuum Mech Therm* 2022; 34(5): 1087–1111.
[66] Sugar, J, and Macsai, MS. What causes keratoconus? *Cornea* 2012; 31(6): 716–719.
[67] Zhang, H, Scarcelli, G, and Randleman, JB. Comparison of superior and inferior corneal biomechanics by polarization-sensitive Brillouin microscopy. *Invest Ophth Vis Sci* 2024; 65(7): 2060–2060.
[68] Debourdeau, E, Planells, G, Chamard, C, et al. New keratoconus risk factors: a cross-sectional case—control study. *Journal of Ophthalmology* 2022; 2022(1): 6605771.

[69] Krachmer, JH, Feder, RS, and Belin, MW. Keratoconus and related noninflammatory corneal thinning disorders. *Surv Ophthalmol* 1984; 28(4): 293–322.

[70] Giorgio, I. A variational formulation for one-dimensional linear thermoviscoelasticity. *Math Mech Complex Syst* 2022; 9(4): 397–412.

[71] Cuomo, M, Contrafatto, L, and Greco, L. A cohesive interface model with degrading friction coefficient. *Math Mech Complex Syst* 2024; 12(2): 113–133.

[72] Altenbach, H, and Eremeyev, V. Thin-walled structural elements: classification, classical and advanced theories, new applications. *Shelllike Struct Adv TheorAppl*. Epub ahead of print 10 August 2016. DOI: 10.1007/978-3-319-42277-0_1.

[73] Altenbach, H, and Eremeyev, V. On the effective stiffness of plates made of hyperelastic materials with initial stresses. *Int J Non Linear Mech* 2010; 45(10): 976–981.

[74] Altenbach, H, Eremeyev, VA, and Naumenko, K. On the use of the first order shear deformation plate theory for the analysis of three-layer plates with thin soft core layer. *Z Angew Math Mech* 2015; 95(10): 1004–1011.

[75] Fedele, R. Third-gradient continua: nonstandard equilibrium equations and selection of work conjugate variables. *Math Mech Solids* 2022; 27(10): 2046–2072.

[76] Fedele, R. Deformation-induced coupling of the generalized external actions in third-gradient materials. *Z Angew Math Phys* 2022; 73(5): 218.

[77] De Angelo, M, Barchiesi, E, Giorgio, I, et al. Numerical identification of constitutive parameters in reduced-order bi-dimensional models for pantographic structures: application to out-of-plane buckling. *Arch Appl Mech* 2019; 89(7): 1333–1358.

[78] Vazic, B, Abali, BE, Yang, H, et al. Mechanical analysis of heterogeneous materials with higher-order parameters. *Eng with Comput* 2022; 38(6): 5051–5067.

[79] Abali, BE, Klunker, A, Barchiesi, E, et al. A novel phase-field approach to brittle damage mechanics of gradient metamaterials combining action formalism and history variable. *Z Angew Math Mech* 2021; 101(9): e202000289.

[80] Placidi, L, Barchiesi, E, and Misra, A. A strain gradient variational approach to damage: a comparison with damage gradient models and numerical results. *Math Mech Complex Syst* 2018; 6(2): 77–100.

[81] Placidi, L, Barchiesi, E, Misra, A, et al. Micromechanics-based elasto-plastic–damage energy formulation for strain gradient solids with granular microstructure. *Continuum Mech Therm* 2021; 33(5): 2213–2241.

[82] Placidi, L, Misra, A, and Barchiesi, E. Two-dimensional strain gradient damage modeling: a variational approach. *Z Angew Math Phys* 2018; 69: 1–19.

[83] Cuomo, M. Continuum damage model for strain gradient materials with applications to 1D examples. *Continuum Mech Therm* 2019; 31(4): 969–987.

[84] Naumenko, K, and Eremeyev, VA. A non-linear direct peridynamics plate theory. *Compos Struct* 2022; 279: 114728.

[85] Placidi, L, Greco, L, Bucci, S, et al. A second gradient formulation for a 2D fabric sheet with inextensible fibres. *Z Angew Math Phys* 2016; 67: 1–24.

[86] Pideri, C, and Seppecher, P. A second gradient material resulting from the homogenization of an heterogeneous linear elastic medium. *Continuum Mech Therm* 1997; 9: 241–257.

[87] Eremeyev, VA, dell'Isola, F, Boutin, C, et al. Linear pantographic sheets: existence and uniqueness of weak solutions. *J Elasticity* 2018; 132: 175–196.

[88] Trinh, DK, Janicke, R, Auffray, N, et al. Evaluation of generalized continuum substitution models for heterogeneous materials. *Int J Multiscale Com* 2012; 10(6).

[89] Eremeyev, VA, Freidin, AB, Pavlyuchenko, VN, et al. Instability of hollow polymeric microspheres upon swelling. *Dokl Phys* 2007; 52(1): 37–40.

[90] Soize, C. An overview on uncertainty quantification and probabilistic learning on manifolds in multiscale mechanics of materials. *Math Mech Complex Syst* 2023; 11(1): 87–174.

[91] La Valle, G, Ciallella, A, and Falsone, G. The effect of local random defects on the response of pantographic sheets. *Math Mech Solids* 2022; 27(10): 2147–2169.

[92] Mühlich, U, Abali, BE, and dell'Isola, F. Commented translation of Erwin Schrödinger's paper 'On the dynamics of elastically coupled point systems'(Zur Dynamik elastisch gekoppelter Punktsysteme). *Math Mech Solids* 2020; 26(1): 1081286520942955.

[93] Mandadapu, KK, Abali, BE, and Papadopoulos, P. On the polar nature and invariance properties of a thermomechanical theory for continuum-on-continuum homogenization. *Math Mech Solids* 2021; 26(11): 1581–1598.

[94] Eremeyev, V, and Pietraszkiewicz, W. Thermomechanics of shells undergoing phase transition. *J Mech Phys Solids* 2011; 59(7): 1395–1412.

[95] Eremeyev, VA, and Pietraszkiewicz, W. Phase transitions in thermoelastic and thermoviscoelastic shells. *Arch Mech* 2009; 61(1): 41–67.

[96] Eremeyev, VA, and Konopińska-Zmysłowska, V. On the correspondence between two-and three-dimensional Eshelby tensors. *Continuum Mech Therm* 2019; 31: 1615–1625.

[97] Abali, BE, and Barchiesi, E. Additive manufacturing introduced substructure and computational determination of metamaterials parameters by means of the asymptotic homogenization. *Continuum Mech Therm* 2021; 33: 993–1009.

[98] Vazic, B, Abali, BE, and Newell, P. Generalized thermo-mechanical framework for heterogeneous materials through asymptotic homogenization. *Continuum Mech Therm* 2023; 35(1): 159–181.
[99] Yang, H, Abali, BE, Müller, WH, et al. Verification of asymptotic homogenization method developed for periodic architected materials in strain gradient continuum. *Int J Solids Struct* 2022; 238: 111386.
[100] Aydin, G, Sarar, BC, Yildizdag, ME, et al. Investigating infill density and pattern effects in additive manufacturing by characterizing metamaterials along the strain-gradient theory. *Math Mech Solids* 2022; 27: 2002–2016.
[101] Sarar, BC, Yildizdag, ME, and Abali, BE. Comparison of homogenization techniques in strain gradient elasticity for determining material parameters. In: Altenbach, H, Berezovski, A, dell'Isola, F, et al. (eds) *Sixty shades of generalized continua: dedicated to the 60th birthday of Prof. Victor A. Eremeyev*. Cham: Springer, 2023, pp. 631–644.
[102] Eremeyev, VA. Two-and three-dimensional elastic networks with rigid junctions: modeling within the theory of micropolar shells and solids. *Acta Mech* 2019; 230(11): 3875–3887.
[103] Altenbach, H, and Eremeyev, VA. *Cosserat-type shells*. Vienna: Springer, 2013.
[104] Eremeyev, VA, and Pietraszkiewicz, W. Nonlinear resultant theory of shells accounting for thermodiffusion. *Continuum Mech Therm* 2021; 33: 893–909.
[105] Eremeyev, VA, and Pietraszkiewicz, W. Local symmetry group in the general theory of elastic shells. *J Elasticity* 2006; 85: 125–152.
[106] Eremeyev, V, and Zubov, L. On constitutive inequalities in nonlinear theory of elastic shells. *Z Angew Math Mech* 2007; 87(2): 94–101.
[107] Ma, H, Gao, XL, and Reddy, J. A non-classical Mindlin plate model based on a modified couple stress theory. *Acta Mech* 2011; 220(1): 217–235.
[108] Abali, BE, Müller, WH, and dell'Isola, F. Theory and computation of higher gradient elasticity theories based on action principles. *Arch Appl Mech* 2017; 87(9): 1495–1510.
[109] Shekarchizadeh, N, Abali, BE, and Bersani, AM. A benchmark strain gradient elasticity solution in two-dimensions for verifying computational approaches by means of the finite element method. *Math Mech Solids* 2022; 27(10): 2218–2238.
[110] Placidi, L, El Sherbiny, MG, and Baragatti, P. Experimental investigation for the existence of frequency band gap in a microstructure model. *Math Mech Complex Syst* 2022; 9(4): 413–421.
[111] Bersani, AM, Caressa, P, and Ciallella, A. Numerical evidence for the approximation of dissipative systems by gyroscopically coupled oscillator chains. *Math Mech Complex Syst* 2022; 10(3): 265–278.
[112] Osorio-Blanco, ER, Bergueiro, J, Abali, BE, et al. Effect of core nanostructure on the thermo-mechanical properties of soft nanoparticles. *Chem Mater* 2020; 32: 518–528.
[113] Zhang, J, Yang, H, Abali, BE, et al. Dynamic mechanics-modulated hydrogels to regulate the differentiation of stem-cell spheroids in soft microniches and modeling of the nonlinear behavior. *Small* 2019; 15: 1901920.
[114] Wagner, H, Barr, J, Zadnik, K, et al. Collaborative longitudinal evaluation of keratoconus (CLEK) study: methods and findings to date. *Cont Lens Anterior Eye* 2007; 30(4): 223–232.
[115] Fedele, R, Raka, B, Hild, F, et al. Identification of adhesive properties in glare assemblies using digital image correlation. *J Mech Phys Solids* 2009; 57(7): 1003–1016.
[116] Fedele, R, Galantucci, L, and Ciani, A. Global 2D digital image correlation for motion estimation in a finite element framework: a variational formulation and a regularized, pyramidal, multi-grid implementation. *Int J Numer Meth Eng* 2013; 96(12): 739–762.
[117] Fedele, R. Simultaneous assessment of mechanical properties and boundary conditions based on digital image correlation. *Exp Mech* 2015; 55: 139–153.
[118] Claire, D, Hild, F, and Roux, S. A finite element formulation to identify damage fields: the equilibrium gap method. *Int J Numer Method Eng* 2004; 61(2): 189–208.
[119] Spagnuolo, M, Yildizdag, ME, Pinelli, X, et al. Out-of-plane deformation reduction via inelastic hinges in fibrous metamaterials and simplified damage approach. *Math Mech Solids* 2022; 27(6): 1011–1031.
[120] Valmalle, M, Smaniotto, B, Spagnuolo, M, et al. Mesoscale DVC analyses and parameter calibration for pantographic block in 3-point flexure. *Eur J Mech A/Solids* 2023; 101: 105063.
[121] Valmalle, M, Vintache, A, Smaniotto, B, et al. Local–global DVC analyses confirm theoretical predictions for deformation and damage onset in torsion of pantographic metamaterial. *Mech Mater* 2022; 172: 104379.
[122] Maier, G, Bocciarelli, M, Bolzon, G, et al. Inverse analyses in fracture mechanics. *Int J Fracture* 2006; 138(1): 47–73.
[123] Fedele, R, Placidi, L, and Fabbrocino, F. A review of inverse problems for generalized elastic media: formulations, experiments, synthesis. *Continuum Mech Therm* 2024; 36: 1413–1453.
[124] Sutton, M, and Hild, F. Recent advances and perspectives in digital image correlation. *Exp Mech* 2015; 55(1): 1–8.
[125] Hild, F, and Roux, S. Digital image correlation: from displacement measurement to identification of elastic properties–a review. *Strain* 2006; 42(2): 69–80.
[126] Grédiac, M, and Hild, F. *Full-field measurements and identification in solid mechanics*. Hoboken, NJ: John Wiley, 2012.
[127] Germain, P. The method of virtual power in the mechanics of continuous media, I: second-gradient theory. *Math Mech Complex Syst* 2020; 8(2): 153–190.

[128] Alibert, JJ, Seppecher, P, and Dell'Isola, F. Truss modular beams with deformation energy depending on higher displacement gradients. *Math Mech Solids* 2003; 8(1): 51–73.
[129] Bîrsan, M, Shirani, M, and Steigmann, DJ. Convexity conditions for fiber-reinforced elastic shells. *Math Mech Solids*. Epub ahead of print August 20, 2024. DOI: 10.1177/10812865241261485.
[130] Bîrsan, M, Shirani, M, and Steigmann, DJ. The coupled Legendre-Hadamard condition for fiber-reinforced materials: three-dimensional solids and two-dimensional shells. *Continuum Mech Therm* 2025; 37(2): 26.
[131] Shirani, M, Luo, C, and Steigmann, DJ. Cosserat elasticity of lattice shells with kinematically independent flexure and twist. *Continuum Mech Therm* 2019; 31: 1087–1097.
[132] Olive, M, and Auffray, N. Symmetry classes in piezoelectricity from second-order symmetries. *Math Mech Complex Syst* 2021; 9(1): 77–105.
[133] Yildizdag, ME, Demirtas, M, and Ergin, A. Multipatch discontinuous Galerkin isogeometric analysis of composite laminates. *Continuum Mech Therm* 2020; 32: 607–620.
[134] Spagnuolo, M, Yildizdag, ME, Andreaus, U, et al. Are higher-gradient models also capable of predicting mechanical behavior in the case of wide-knit pantographic structures? *Math Mech Solids* 2021; 26(1): 18–29.
[135] Erden Yildizdag, M, Placidi, L, and Turco, E. Modeling and numerical investigation of damage behavior in pantographic layers using a hemivariational formulation adapted for a Hencky-type discrete model. *Continuum Mech Therm* 2023; 35(4): 1481–1494.
[136] Valoroso, N, and Fedele, R. Characterization of a cohesive-zone model describing damage and de-cohesion at bonded interfaces. sensitivity analysis and mode-I parameter identification. *Int J Solids Struct* 2010; 47(13): 1666–1677.
[137] Ponomarev, D. A generalised time-evolution model for contact problems with wear and its analysis. *Math Mech Complex Syst* 2022; 10(3): 279–319.